CALORIMETRIC MODE PHOTON ANALYSIS USING THE ALPHA MAGNETIC SPECTROMETER (AMS-02)

A THESIS SUBMITTED TO
THE GRADUATE SCHOOL OF NATURAL AND APPLIED SCIENCES
OF
MIDDLE EAST TECHNICAL UNIVERSITY

BY

CENK TÜRKOĞLU

IN PARTIAL FULFILLMENT OF THE REQUIREMENTS
FOR
THE DEGREE OF MASTER OF SCIENCE
IN
PHYSICS

FEBRUARY 2015

Approval of the thesis:

CALORIMETRIC MODE PHOTON ANALYSIS USING THE ALPHA MAGNETIC SPECTROMETER (AMS-02)

submitted by **CENK TÜRKOĞLU** in partial fulfillment of the requirements for the degree of **Master of Science in Physics Department, Middle East Technical University** by,

Prof. Dr. Gülbin Dural Ünver _____
Dean, Graduate School of **Natural and Applied Sciences**

Prof. Dr. Mehmet T. Zeyrek _____
Head of Department, **Physics**

Assoc. Prof. Dr. M. Bilge Demirköz _____
Supervisor, **Physics Department, METU**

Examining Committee Members:

Prof. Dr. Mehmet T. Zeyrek
Physics Department, METU _____

Assoc. Prof. Dr. M. Bilge Demirköz
Physics Department, METU _____

Prof. Dr. Altuğ Özpineci
Physics Department, METU _____

Assoc. Prof. Dr. İsmail Turan
Physics Department, METU _____

Prof. Dr. İsmail Boztosun
Physics Department, Akdeniz University _____

Date: _____

I hereby declare that all information in this document has been obtained and presented in accordance with academic rules and ethical conduct. I also declare that, as required by these rules and conduct, I have fully cited and referenced all material and results that are not original to this work.

Name, Last Name: CENK TÜRKOĞLU

Signature :

ABSTRACT

CALORIMETRIC MODE PHOTON ANALYSIS USING THE ALPHA MAGNETIC SPECTROMETER (AMS-02)

Türkoğlu, Cenk
M.S., Department of Physics
Supervisor : Assoc. Prof. Dr. M. Bilge Demirköz

February 2015, 68 pages

Alpha Magnetic Spectrometer (AMS-02) is a particle detector built for the purpose of detecting primordial anti-matter and signals of dark matter. AMS-02 operates as an external module on the International Space Station and will be operational for at least 10 years. For finding traces of the strongest dark matter candidate, neutralino, peaks in the background positron, antiproton and gamma ray flux have to be studied. For this purpose, AMS-02 includes a permanent magnet that bends particles and anti-particles in opposite directions, a tracking system and high precision detectors (Transition Radiation Detector (TRD), Electromagnetic Calorimeter (ECAL)) which identifies electrons and positrons among other cosmic particles. There are two ways to do photon analysis: conversion mode and calorimetric mode. Conversion mode inludes the photons which start their showers in the upper parts of AMS-02 detector. In calorimetric mode, photons which convert into electron-positron pairs after entering Electromagnetic Calorimeter (ECAL) are taken into account. In this thesis, calorimetric photons will be studied above 5 GeV.

Keywords: Alpha Magnetic Spectrometer, AMS-02, Dark Matter, Weakly Interacting Massive Particles, WIMP, Calorimetric Mode, Photon

ÖZ

ALFA MANYETİK SPEKTROMETRESİ (AMS-02) İLE KALORİMETRİK MODDA FOTON ANALİZİ

Türkoğlu, Cenk
Yüksek Lisans, Fizik Bölümü
Tez Yöneticisi : Doç. Dr. M. Bilge Demirköz

Şubat 2015 , 68 sayfa

Alfa Manyetik Spektrometresi (AMS-02), ilkel karşıt madde ve karanlık madde sinyallerini bulmak amacıyla inşa edilmiş bir parçacık dedektörüdür. AMS-02, Uluslararası Uzay İstasyonunda harici bir modül olarak işlev görmektedir ve en az 10 yıl boyunca çalışacaktır. En güçlü karanlık madde adayı olan nötralinonun izlerini bulmak için pozitron, antiproton ve gamma ışınımı akısı arkaplanındaki tepe noktaları çalışılmalıdır. Bu nedenle, AMS-02 parçacıkları ve karşıt parçacıkları farklı yönlerde büken daimi bir mıknatıs, bir iz bulma sistemi ve elektron ile pozitronları diğer kozmik parçacıklar arasında tespit eden yüksek hassaslıkta dedektörler (Geçiş Radyasyonu Dedektörü (TRD), Elektromanyetik Kalorimetre (ECAL)) içermektedir. Foton analizi iki şekilde yapılabilir: dönüşüm modu ve kalorimetrik mod. Dönüşüm modu, duşa AMS-02 dedektörünün üst kısımlarında başlayan fotonları içermektedir. Kalorimetrik modda ise, Elektromanyetik Kalorimetreye (ECAL) girdikten sonra elektron-pozitron çiftine dönüşen fotonlar göz önüne alınmaktadır. Bu tezde, 5 GeV üzeri kalorimetrik modundaki fotonlar çalışılacaktır.

Anahtar Kelimeler: Alfa Manyetik Spektrometresi, AMS-02, Karanlık Madde, Zayıf Etkileşen Devasa Parçacık, WIMP, Kalorimetrik Mod, Foton

To my family

ACKNOWLEDGMENTS

I would like to express my gratitude to my supervisor Prof. Bilge Demirköz knowledge and wisdom of whom changed my course in my master of science education. I couldn't have finished my research and this thesis without her guidance. I would like to thank her for the encouregement and patience she showed me in my whole master of science education.

I would like to express my gratitude to Prof. Ting for letting me work at AMS-02 experiment. Also, I would like to thank all AMS Collaboration members for helping with my research.

I would like to thank my collegues and friends Tansu Daylan, Emirhan Postacı and Emre Ergeçen who besides being really good friends also helped me throughout my analysis. Without their encouragement and friendship, I couldn't have gotten through many obstacles. I would also like to thank Dilek Kızılören, Ramazan Uzel and Ayşenur Gencer for their comments on my analysis and their friendship.

I would like to thank my friend, also my collegue, Karen Andeen who was there for me when I needed help with my analysis. I would like to thank her for her friendship which was very important to me especially when I was at CERN. She was there for me whenever I needed to talk to someone.

I would like to thank my friends Savaş Gayaker, Güneş Biliciler, Mesut Ünal, Deniz Kennedy, Yusuf Kasap, Buğra Bilin, Zekeriya Uysal, Uygar Şaşmaz, Ava Bagherpoor, Damla Çelik, Nilüfer Köse, Beray Yaldız, Murat Öztürk, Selen Saatci and Botan Elveren who helped me through all the stressful periods in my master's education. They were always there for me when I needed someone to talk to. I would like to thank my band members Volkan Acun, Tuğcan Selimhocaoğlu, Mert Doğan, Boray Değerliyurt and Berk Bozkır for their friendship. Without the fun we had in our studio sessions, I couldn't have gotten rid of the stress inflicted upon me.

Last but not least, I would like to thank my mother Şennur Türkoğlu for her continuous support and belief in me. Without her, this thesis may not have seen the light of day. Also, I would like to thank my father Orhan Türkoğlu for believing in me until his last breath. He lives in my heart and will do so until my last breath.

This work is partially supported by Turkish Atomic Energy Agency (TAEK) under the grant agreement 2012TAEKCERN-A5.H2.P1.01-20, and by the Marie Curie Career Integration Grants (CIG) under the grant agreement PCIG10-GA-2011-304264.

TABLE OF CONTENTS

LIST OF FIGURES

FIGURES

LIST OF ABBREVIATIONS

ACC	Anticoincidence Counters
AMS	Alpha Magnetic Spectrometer
CAST	CERN Axion Solar Telescope
CERN	The European Organization for Nuclear Research
CMB	Cosmic microwave background
COBE	Cosmic Background Explorer
ECAL	Electromagnetic Calorimeter
ESA	European Space Agency
IACT	Imaging Air Čerenkov Telescopes
ISS	International Space Station
LHC	Large Hadron Collider
LSP	Lightest supersymmetric particle
MC	Monte Carlo
MIP	Minimum ionizing particle
NASA	National Aeronautics and Space Administration
PAMELA	a Payload for Antimatter Matter Exploration and Light-nuclei Astrophysics
PMT	Photomultiplier Tube
QCD	Quantum Chromodynamics
RICH	Ring Imaging Čerenkov Detector
SAA	South Atlantic Anomaly
SM	Standard Model
SUSY	Supersymmetry
TAS	Tracker Alignment System
TOF	Time of Flight System
TR	Transition radiation
TRD	Transition Radiation Detector
WIMP	Weakly interacting massive particle

CHAPTER 1

INTRODUCTION

The Alpha Magnetic Spectrometer (AMS-02) is an astroparticle physics experiment which was placed on the International Space Station (ISS) on 16th of May, 2011 and has been collecting cosmic ray data since 19th of May, 2011. AMS-02 is orbiting the Earth on the ISS at an altitude between $300 - 400\ km$. The position of AMS-02 can be seen after it was installed on the ISS in Figure 1.1. The main objective of AMS-02 is to search for a dark matter signature and primordial anti-matter nuclei.

AMS-02 has several subdetectors such as Tracker, Electromagnetic Calorimeter, Transition Radiation Detector, Time of Flight Detector, Ring Imaging Cherenkov Detector and a permanent magnet. AMS-02 can measure momentum of the charged particles up to $3\ TeV/nucleon$ and can also determine the charge by reconstructing the curvature of the particle tracks inside the magnetic field. Energy of the electromagnetically interacting particles such as electrons, positrons and photons can be reconstructed using the Electromagnetic Calorimeter. In addition, the incoming direction can be found from the shower shape. The energy spectra of antiprotons, positrons and gamma rays may possibly contain signatures of dark matter annihilation in the galactic halo.

AMS-02 collected more than 55 billion cosmic ray events for 1246 days as of 16th of October, 2014 and is planned to continue its operation on the ISS until 2024, which has already been approved. First publication of AMS-02 was on the measurement of the positron fraction between $0.5 - 350\ GeV$ using 8% of the expected total data [14]. The latest publications are about positron fraction between $0.5 - 500\ GeV$ [5], separate electron and positron fluxes between $0.5 - 700\ GeV$ [12] and combined electron and positron fluxes between $0.5\ GeV - 1\ TeV$ [13].

There are two analysis groups in the AMS-02 collaboration named Group A and Group Alpha. These groups work on every analysis subject separately and they present their work at monthly collaboration meetings. After these analyses are discussed and the collaboration reaches a consensus, then the analysis is finished and is published. The METU-AMS team takes part in the Alpha analysis group with the other member institutes such as MIT, LAPP-Annecy, Hawaii, Grenoble, IHEP-Beijing, Academia Sinica, CIEMAT-Madrid and Geneva.

Figure 1.1: A photo of AMS-02 (right bottom) after it was installed on the ISS. In this picture, taken on July 12 ,2011, radiators and solar panels of ISS can be seen as well. This photo was taken during a space walk by the astronauts living on ISS [48].

In this thesis, a calorimetric photon mode analysis is presented using the cosmic ray data from AMS-02. A signal related to the annihilation of dark matter in the galactic halo may be observed as a sharp peak in the photon spectrum [30]. In Chapter 2, the observational evidence and current theories on dark matter are presented. In Chapter 3, subdetectors, subsystems and performance of the AMS-02 detector along with the published results are presented. The calorimetric mode photon analysis is described in detail in Chapter 4 and a conclusion is given in Chapter 5.

CHAPTER 2

DARK MATTER

In this chapter, observational evidence of dark matter will be presented briefly. Particle nature of dark matter and different possible detection mechanisms, specifically detecting the annihilation into photons, will be discussed. In the last section, the interaction of photons in detector material will be presented.

2.1 Observational Evidence

There are various observational evidence for the existence of dark matter. The first evidence came from a Swiss astrophysicist Fritz Zwicky who was looking for the dispersion speed of a group of seven galaxies in the Coma Cluster in 1933. The discrepancy he found between the dynamical and luminous masses of the galaxies led him to conclude that there might exist extra mass which does not emit light, hence he called it dark matter [58].

In 1970, Vera Rubin carried out measurements of the velocity curve of the spiral galaxies [46] and she found out that galactic rotational curves were flat; they didn't show the expected decrease at large radii [45]. She suggested that this could be explained by dark matter having a halo shape and its contribution may be the reason for this flatness.

The observation of Bullet Cluster, two colliding galaxies, demonstrates that the center of the baryonic mass and the centre of the total mass can be spatially different, providing a rare visual tool for understanding dark matter [28].

Cosmic Microwave Background (CMB) radiation, the thermal radiation filling the Universe, provides a measurement of the dark matter content of the Universe. According to the results of Planck Space Telescope of European Space Agency (ESA), the Universe consists of 4.9% atoms, 26.8% dark matter and 68.3% dark energy [9].

Cold dark matter is the theory that is seen as the most likely dark matter candidate by cosmologists because it gives the best description of observed phenomena as the Universe evolves from small structures to galaxy clusters. This theory has been favoured since 2006 [18].

2.2 Dark Matter as a Particle

Cold (non-relativistic) non-baryonic dark matter particles are the leading candidates for particle nature of dark matter. There are two strong candidates for cold non-baryonic dark matter: axions and weakly interacting massive particles (WIMP).

The theory of axions arise from a possible solution to the strong CP problem in QCD [43]. The mass of the axions is constrained to the scale of $10^{-5}\ eV$ [37].

The other candidates for dark matter are WIMPs which are very stable and which can arise in different extensions to the Standard Model such as hidden valley theories and supersymmetry (SUSY).

The significance of SUSY comes from the fact that it naturally relates fermions and bosons through a symmetry. According to SUSY, each Standard Model boson has a fermion superpartner and vice versa. In several versions of SUSY theories, the lightest supersymmetric particle (LSP) neutralino is the most theoretically developed WIMP candidate. LSP is predicted to be stable by an exact discrete symmetry called R-parity. Linear combinations of superpartners of photon, Higgs and Z called photino, Higgsino and Zino, respectively, make the neutralino. It is predicted that the mass of the neutralino should not be more than a few TeV and it should interact weakly with baryonic matter. The cosmological abundance should be $\Omega \sim 1$ if a WIMP as neutralino exists. This should also correspond to the existing dark matter content in the Universe [37]. If WIMPs are the reason for the flatness of the galac-

tic rotation curves, this can have two implications. One of these implications is that local halo density should be about $0.3\ GeVcm^{-3}$. The other implication is that they should have a velocity dispersion about $220\ km\ s^{-1}$ and have a Maxwell-Boltzmann distribution [37].

2.3 Dark Matter Detection

The interaction of WIMPs with ordinary matter occurs through three different mechanisms. These mechanisms are scattering (direct detection), production (collider) and annihilation (indirect detection) as shown in Figure 2.1. In order to test these mechanisms, different experiments should be conducted. All three of these methods need to be established before physicists can claim that dark matter particle has been discovered. In direct detection experiments, scattering of dark matter particles from baryonic matter is investigated. Collider searches aim to produce dark matter particles and detect them through missing transverse energy in their detectors. Experiments involving indirect measurements look for the excess particles coming from the annihilation of dark matter particles.

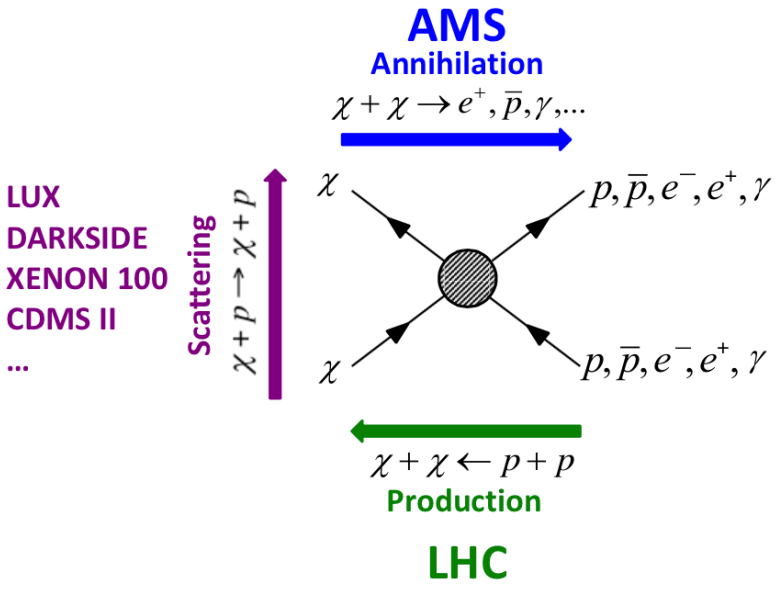

Figure 2.1: Different dark matter detection mechanisms [53].

Since WIMPs are predicted to have low velocity, elastic scattering of spin independent interactions are considered as the dominant mechanism of their interactions [47]. The

reason scattering experiments are conducted underground is that cosmic ray background is reduced compared to laboratories above the ground. Noble liquid detectors and cryogenic detectors with carefully selected non-radioactive isotopes are the most common types used for direct detection. Noble liquid detectors looks for the flash of the scintillation light generated by the collision of a particle with the noble liquid like argon or xenon. Cryogenic detectors work at temperatures less than ~$100\ mK$ in order to detect the heat generated after a particle hits an atom in the crystal absorber such as germanium.

The signal for dark matter particles can be found in accelerator based collider experiments, like LHC, through the missing transverse energy (MET). There are searches for dark matter from CMS (Compact Muon Solenoid) [38] and ATLAS (A Toroidal LHC ApparatuS) [2] experiments. These searches are based on different SUSY models and masses up to $700\ GeV$ have been ruled out in several of them [1].

As for indirect searches, standard model particles can be produced in the annihilation of dark matter in the Galactic Halo. If dark matter particles collide in the galactic halo, they can annihilate into SM particle anti-particle pairs like W^-W^+, ZZ, $\tau^-\tau^+$, HH,$t\bar{t}$ etc. These particles will then decay into the few stable particles known such as $e\pm$, p, $\bar{p}$, ν, $\bar{\nu}$ and γ. These mechanisms can be shown as follows:

$$\begin{aligned} \chi + \chi &\rightarrow \bar{p} + ... \\ &\rightarrow e^+ + ... \\ &\rightarrow \gamma + ... \end{aligned}$$

Protons and electrons are abundant in cosmic rays and finding a dark matter signature in them could prove formidable. If a deviation occurs from the expected power law spectrum for rarer particles such as anti-protons, positrons and gamma rays, this can hint a signal of dark matter. One of the most interesting research on cosmic rays is positron fraction. A publication by PAMELA shows the positron fraction with 24500 positron events observed during a three and a half year period [10]. Also, AMS-02 published two papers on positron fraction, which will be discussed thoroughly in Chapter 3, with more statistics and a higher energy range.

Neutrinos are extremely difficult to detect and there are a couple of experiments searching for high energy neutrinos. ICECUBE experiment is one of these experi-

ments. ICECUBE is a neutrino observatory buried 2500 meters deep in Amundsen-Scott South Pole Station [50]. ICECUBE put an upper limit for the cross-section with respect to the WIMP mass in between $300\ GeV - 100\ TeV$ for the $\nu\bar{\nu}$ annihilation [3].

2.4 Dark Matter Signals Through Gamma Rays

Gamma rays play a dramatic role in the search for a dark matter signal. The difference of gamma rays from charged particles is that they do not have electrical charge. Gamma rays travel from their sources without being affected by the magnetic field. In this way, gamma rays can be traced back to their origin and the coordinates at which possible dark matter annihilations occur can be determined [22].

Given that the kinetic energy of dark matter particles are low, the spectrum of these photons must have a soft cut-off at the kinematical limit at $E_\gamma = m_\chi$ where m_χ stands for the mass of the dark matter particle. It is highly probable for the electrons and positrons produced from the dark matter annihilations to generate gamma rays through the processes such as Bremsstrahlung and inverse Compton scattering. This leads to a non-negligible contribution to the low energy photon spectrum from the annihilations of dark matter occuring near the Galactic Plane [31]. A possible way of detecting dark matter is to look for a broad bump-like structure on the spectrum [23]. However, since the expected photon flux is generally weak when compared to the astrophysical sources, striking signatures from the experiments become valuable in trying to recognize a signal. Detecting a narrow photon line that originates from dark matter particles annihilating into $\gamma\chi$, where χ could be a gamma ray, a Higgs boson, a Z boson or a particle that is not from SM, could be considered as a distinctive signal [4]. Another drawback in the search for photons in cosmic rays is their abundances compared to the other cosmic particles.

For each positron in cosmic rays, there are 100.000 protons and for each anti-proton, there are 100 electrons. This makes the distinction between positron/proton and electron/anti-proton crucial for such searches [48]. However, the ratio of photons to protons is much lower than the ratio of positrons to protons. The number of pho-

tons is substantially small since a huge percentage of the cosmic rays is protons. Consequently, this makes protons the greatest background in photon research.

There are two ways to observe gamma rays: directly from space or from ground based experiments. The first one is trying to detect photons passing through a detector in space. These experiments have small effective areas and because of the limits on the resolution, have upper bounds on the gamma ray energies they are able to detect. However, photons at relatively small energies can be observed and the field of view is larger compared to the second option which is ground based experiments. Imaging Air Čerenkov Telescopes (IACTs) can detect Čerenkov light emitted by the shower of particles starting in the upper atmosphere and use image reconstruction algorithms for determining the features of the primary gamma ray. These experiments are good at pointed observations because of their small field of view and large effective area. However, they have a lower bound on the energy for making distinction between the gamma rays and background particles such as protons and muons [23].

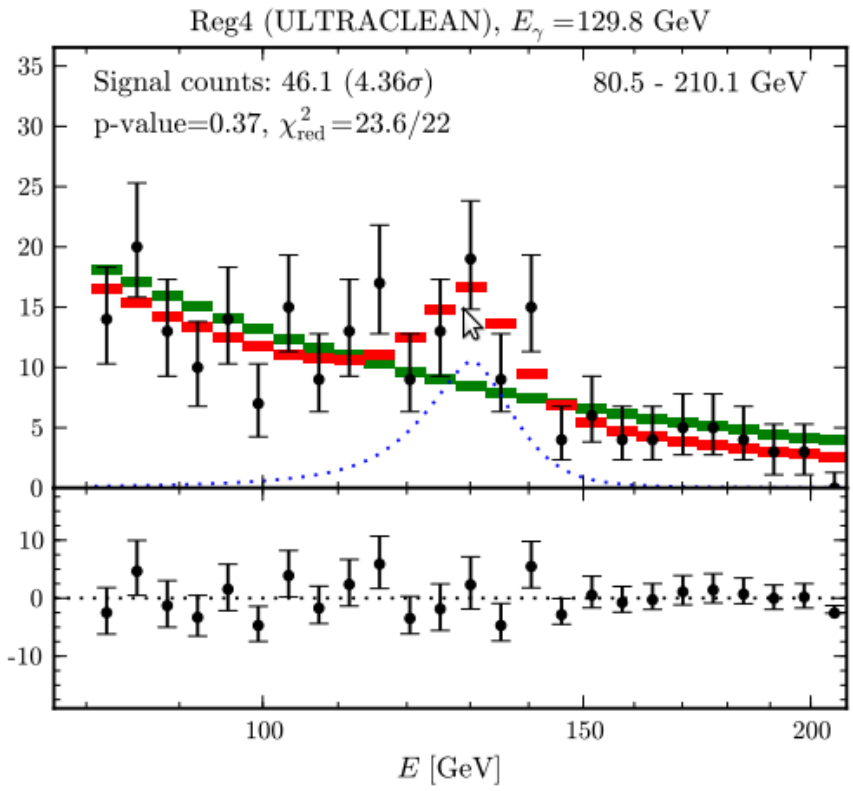

Figure 2.2: A claimed deviation from the power law spectrum at 129.8 GeV from the observations of FERMI LAT is shown [56].

FERMI LAT claimed to have observed a deviation in the power law spectrum approximately at $130\ GeV$ in the area close to the Galactic Center. This signal was based on 50 photons. If this signal is to be interpreted as dark matter particles annihilating each other and give out photon pairs, then the measurements show that the mass of the dark matter should be $m_\chi = 129.8 \pm 2.4\ GeV$. Figure 2.2 shows the spectrum around this energy level as observed by FERMI LAT [56].

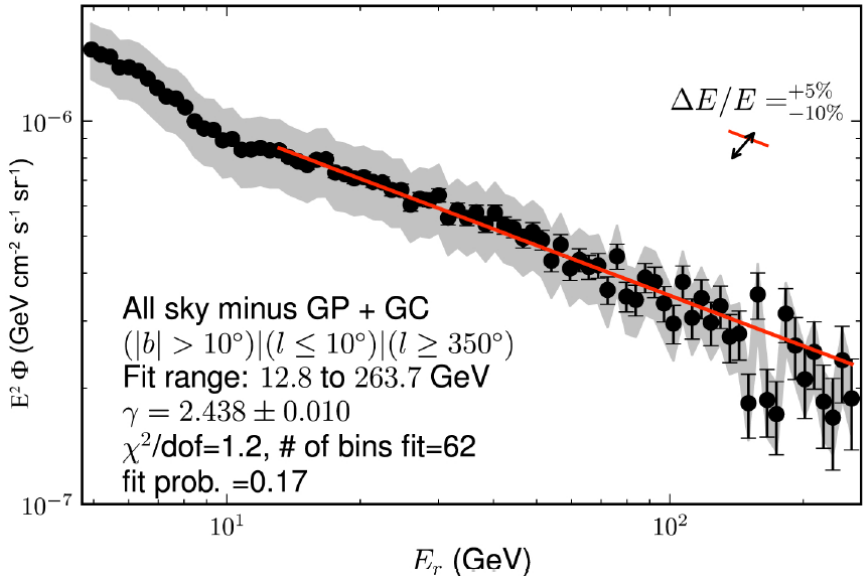

Figure 2.3: Gamma ray flux measured by FERMI LAT multiplied by E^2 is drawn with respect to the energy. A power law fit, in red, corresponding to the measurements is also shown. The gray area stands for the systematic uncertainty of the analysis [8].

Another publication by FERMI LAT shows gamma ray flux measurement up to the energy $263.7\ GeV$ and it is shown in Figure 2.3 It was fitted with a power law [8].

2.5 Interaction of Photons in Detector Material

The analysis conducted for this thesis is on the photons showering in the calorimeter of AMS-02. Photons create positron-electron pairs when they interact in matter and this phenomenon is known as the pair production. These electrons and positrons then shower electromagnetically.

Electromagnetic shower is a process in which longitudinal development is dominated by three different processes. The formation of the shower is caused by pair production

and Bremsstrahlung whereas the expiration occurs due to the ionisation of atoms [19]. When a highly energetic gamma ray converts to $e^{\pm}$, these particles then emit Bremsstrahlung photons. If they have enough energy, these photons converts to $e^{\pm}$ pairs again and this process continues until the energy of the electrons drop below the critical energy E_c defined as the energy at which energy loss of electrons by ionization of the material molecules becomes the dominant process [51].

The showering process can be constructed as a simple model using the radiation length which will be explained later in this section. A photon with energy E_0 will convert into an $e^{\pm}$ pair approximately after one radiation length. Both electron and positron will have the same energy which is $E_0/2$. After another radiation length, this will be followed by release of Bremsstrahlung photons from the $e^{\pm}$ pair which will double the total number of particles with two photons and an $e^{\pm}$ pair. The photons and the pair will have approximately equal energies that is equal to $E_0/4$. Then, at the third radiation length, these Bremsstrahlung photons will pair produce and the total number of particles in the cascade will be equal to 8. Figure 2.4 shows an example of an electromagnetic cascade. Continuing this process, the number of particles can be calculated using the total number of radiation lengths before the shower dies:

$$N = 2^t \tag{2.1}$$

where t is the number of radiation lengths. Also, the average energy can be calculated using:

$$E(t) \simeq \frac{E_0}{t} \tag{2.2}$$

The result wouldn't have differed if the starting particle was an electron or a positron. In addition, maximum penetration depth of the shower can be calculated as well if it is assumed that the shower stops at E_c:

$$E(t_{max}) = \frac{E_0}{2^{t_{max}}} = E_c \tag{2.3}$$

If this equation is solved for t_{max}:

$$t_{max} = \frac{ln\frac{E_0}{E_c}}{ln2} \tag{2.4}$$

Then, maximum number of particles can be calculated as follows:

$$N_{max} \simeq \frac{E_0}{E_c} \tag{2.5}$$

This calculation gives an approximate picture of the showering process. However, in reality, the number of particles rises exponentially and peak at a broad maximum, then decreases slowly.

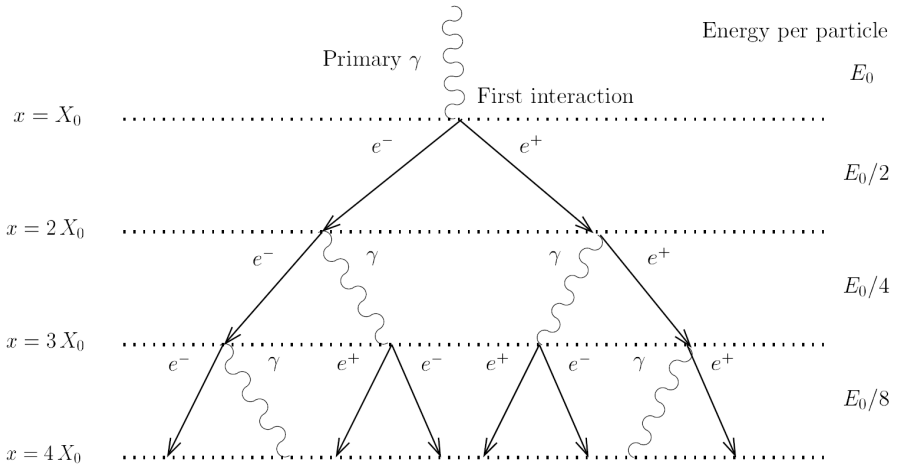

Figure 2.4: A photon showering through pair production and the converted $e^{\pm}$ pair through Bremsstrahlung. An electromagnetic cascade is developed by these two processes [19].

Pair production is a process in which a photon transforms into an electron-positron pair. This process can only happen in the presence of a third body like a nucleus to conserve the momentum. For a photon to pair produce, it should have at least $1.022\ MeV$ energy.

Pair production is related to the Bremsstrahlung theoretically if a substitution rule is used. When the calculations for one process is carried out, the results related to the other one follows. In the case of Bremsstrahlung, electrons screening the nucleus has an important part in pair production.

Mean free path, λ_{pair}, of a photon for pair production can be calculated using the total cross-section which depends on Z, as follows [40]:

$$\lambda_{pair} = \frac{1}{N\tau_{pair}} \tag{2.6}$$

where N stands for the density of the atoms and τ_{pair} stands for the pair production cross-section of a photon. From mean free path, radiation length can be calculated. Radiation length is a material characteristic which gives information about the energy loss of high energy electromagnetically interacting particles such as positrons,

electrons and photons. High energy positrons and electrons lose energy in matter via Bremsstrahlung and photons via pair production. The amount of material passed for these interactions to occur is defined as the radiation length and it is measured in g/cm^2. Radiation length is shown with X_0 and its relation with the mean free path is as follows [40]:

$$X_0 \simeq \frac{7}{9}\lambda_{pair} \tag{2.7}$$

For positrons and electrons, it is defined as the mean distance at which the particle loses its energy by Bremsstrahlung until 1/e of it is left. For photons, it is defined as the 7/9 of the mean free path in which pair production occurs [51].

In the next chapter, AMS-02 with special emphasis on the calorimeter, which has a radiation length of 17 X_0, will be presented.

CHAPTER 3

AMS-02 EXPERIMENT

In this chapter, AMS-02 experiment and the different analysis methods for photons will be discussed and the current publications of AMS-02 will be presented.

3.1 AMS-02 on the ISS

AMS-02 is a multi-purpose particle detector and its blown-up view can be seen in Figure 3.1. It was delivered to the International Space Station with the space shuttle Endeavour on May 16, 2011. After it was stationed on the ISS on May 19, 2011, the AMS-02 started taking data. Currently, AMS-02 is travelling around the Earth on the ISS at an altitude between 300 and 400 km. It has collected more than 56 billion events so far.

AMS-02 has five subdetectors and a permanent magnet. Transition Radiation Detector (TRD), can identify electrons and positrons among protons. Silicon Tracker, with the help of the permanent magnet, can identify the rigidity and the charge of the particle. Time of Flight (ToF) detector can measure the charge and the velocity of the charged particles. Ring Imaging Čerenkov Detector (RICH) can measure the velocity, the charge and with the help of the Silicon Tracker, the mass of the charged particle. Electromagnetic Calorimeter (ECAL) can measure the energy and the direction of the electromagnetically showering particles.

The coordinate system of AMS-02 is defined such that the $\hat{z}$ is the axis points from the centre to the top. The direction of a downgoing particle in the AMS-02 coordinate

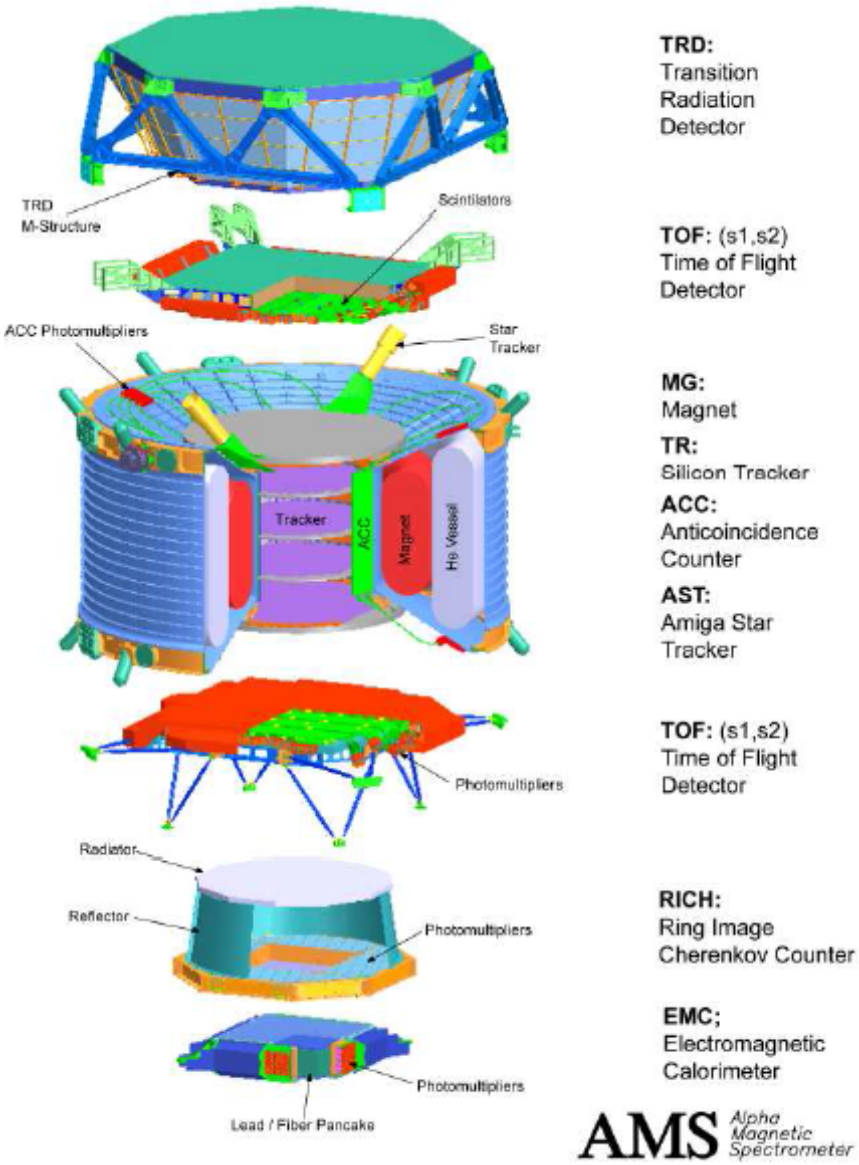

Figure 3.1: The blown-up view of AMS-02 showing the sub detectors and the sub systems [32]

system is defined as $\hat{z} = -1$. Magnetic field of AMS-02 points in the $+\hat{x}$ direction which bends the charged particles in the $\pm\hat{y}$ directions. Therefore, y - z plane is called the bending plane.

Now, a short description of the subdetectors will be given.

3.1.1 Subdetectors

3.1.1.1 Anti Coincidence Counter

While AMS-02 is optimized to take data for downgoing particles, in space, particles come from all directions. Particles coming from the sides could cause complications for analysis because they might leave hits in the tracker which can lead to the mis-reconstruction of the track and consequently, the charge. In order to eliminate this possibility, an anti coincidence counter was placed around the tracker and it vetoes charged particles coming from the sides. ACC is formed from sixteen $8mm$ thick scintillating panels [49]. The particles coming from around the magnet are eliminated using the time information while the back scattered particles coming from the inside of AMS-02 acceptance are accepted as shown in Figure 3.2.

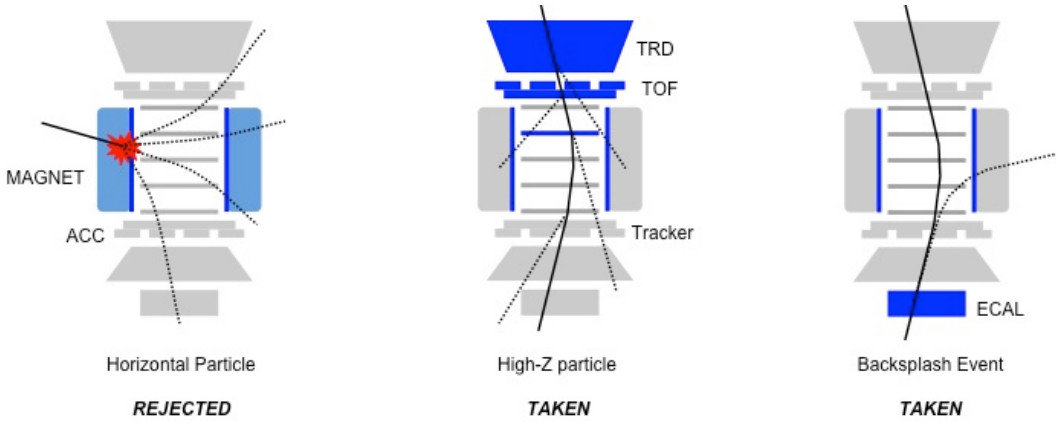

Figure 3.2: Working principle of the Anti Coincidence Counter (ACC). If particles coming from the conversion of a high Z particle or back splashed events hit ACC from inside, these particles are accepted whereas particles hitting ACC from outside are rejected [48].

3.1.1.2 Silicon Tracker and Magnet

The observable difference between a particle and its anti-particle is its charge. Silicon Tracker, with the help of the permanent magnet, is responsible for making this distinction. Charged particles bent by the magnet are reconstructed as tracks in the

tracker and give the rigidity information defined by the following:

$$R = \frac{P}{Z} \tag{3.1}$$

where R is rigidity, P is momentum and Z is the charge. Since the magnetic field of the permanent magnet is known accurately and the curvature of the particle is measured, the rigidity is calculated with the equation

$$R = B \cdot r \tag{3.2}$$

where B stands for the magnetic field and r for the curvature.

Silicon Tracker has nine layers. Upper tracker layer is situated at the top of the TRD and the lower between the RICH and the ECAL whereas the other seven layers are inside the volume of the magnet and the ACC. Each layer is constructed out of ladders that are made up of the groups of double-sided micro-strip silicon sensors volume of each is $41.360 \times 72.045 \times 0.300\ mm^3$ [24]. The spatial resolution for the tracker in the bending yz plane is 10 μm whereas in the xz plane it is 30 μm. The magnet is made from Neodymium-Iron-Boron [49] and has a 0.14 T magnetic field [27]. The magnetic dipole moment outside the magnet is of negligible scale [49].

Tracker tracks are reconstructed out of these hits. By minimizing the fit residuals, rigidity of the charged particle is calculated [49]. As track rigidity increases, a small deviation from a straight line determines the charge of the particle. How well the tracker planes are aligned becomes the dominating source of systematic error for high energy rigidity measurements. The Tracker Alignment System (TAS) monitors geometrical stability of the tracker. Measured misalignments are then corrected offline [48].

3.1.1.3 Transition Radiation Detector

The tracker cannot differentiate between both positively charged protons and positrons with the same momentum. Besides a calorimeter, the only detector that can differentiate between a high energy positron and a proton is the TRD. When an ultra relativistic ($\gamma \geq 300$) charged particle crosses from one media to another media each with different dielectric constants, transition radiation in the range of X-rays is emitted and

can be detected to differentiate between a $100\ GeV$ positron which has $\gamma = 195167$ and a $100\ GeV$ proton which has $\gamma = 106$ [24].

The TRD is constructed from 20 layers of alternating radiator material which consists of thick fibre fleece with 20 mm thickness and 0.06 $\frac{g}{cm^3}$ density and gas proportional tube detectors. Of these 20 layers, the upper and the lower 4 layers give information in the $\hat{x}$ while 12 in the middle give information in the $\hat{y}$ direction. The proportional tubes are filled with $Xe : CO_2$ with the ratio $90 : 10$ [20]. The discrimination between $e^{\pm}$ and protons is achieved by combining the signals from all of the layers of the TRD in a TRD estimator constructed from the ratio of the log-likelihood probability of $e^{\pm}$ to the log-likelihood probability of protons using the hypothesis for these particles. The rejection power for protons using the TRD estimator at an $e^{\pm}$ efficiency of 90% measured on orbit is approximately 10^3 at $110\ GeV$ [39].

3.1.1.4 Ring Imaging Čerenkov Detector

RICH is a subdetector which can measure the velocity of the particle. When a particle traverses a medium at high velocities, its speed in that medium can be greater than the speed of light in that medium while being smaller than c in the vacuum. This particle emits light in the shape of a cone named the Čerenkov effect. From the angle of the cone, the speed of the particle is calculated using the refractive index of the material used to construct the RICH radiator. The formula for the calculation of the velocity from the angle is as follows:

$$\theta_C = \frac{1}{n\beta} \tag{3.3}$$

θ_C stands for the Čerenkov angle and n for the refractive index of the material. β means $\frac{v}{c}$ from which the velocity of the particle is retrieved [25].

Another important aspect of the RICH is that it gives the mass information indirectly when used together with the tracker and the ToF. Cosmic rays include charged heavy nuclei, which differ in masses. If the mass is measured, heavy nuclei can be identified with great precision. The equation used to calculate mass is as follows:

$$m = \frac{R \cdot Z}{\beta \cdot c} \cdot \sqrt{1 - \beta^2} \tag{3.4}$$

R stands for rigidity retrieved from the tracker and Z stands for the charge retrieved from the tracker, ToF or RICH. β is the ratio of the velocity of the particle to the speed of light c.

The velocity resolution estimated for RICH is $\delta\beta = 10^{-3}$ for a $\beta = 1$ and $Z = 1$ particle and it increases up to the limit of $\delta\beta = 5 \cdot 10^{-4}$ with increasing charge [42].

3.1.1.5 Time of Flight

The primary purpose of the ToF detector is to provide a fast trigger for AMS-02. In addition, it can also measure the velocity and the direction of the charged particles and photons that have converted before ToF. The absolute charge can also be measured using ToF which can complement the measurements of the other sub detectors [49]. Figure 3.3 shows the Time of Flight detector before the macro assembly of AMS-02. The ToF can provide timing information of downgoing or back scattered particles which is crucial for calorimetric photon background reduction. Charged particles coming from above the calorimeter can be eliminated and ones coming from the conversions inside ECAL can be retained.

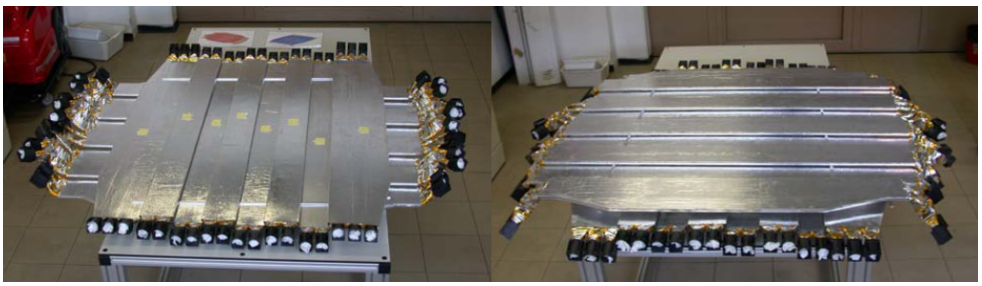

Figure 3.3: The pictures of the upper (left) and lower (right) ToF planes [8].

There are four ToF layers that are made of ploy-vinyl-toluene paddles [42]. Each of these paddles have the dimensions $1 \times 12 \times 120\ cm^3$ and each layer has, starting from the top, 8, 8, 10 and 8 paddles in its structure [48]. Every paddle has two to three photomultiplier tubes at the ends for efficiently detecting particles going through it [20]. Two of these layers are above and two of them are below the magnet. One of

the layers in each pair is in $\hat{x}$ and the other is in $\hat{y}$ directions [48]. The active area of each ToF plane is $1.2m^2$ and the geometrical acceptance for ToF is $0.4m^2$.

The time resolution of each ToF photomultiplier counter is $160ps$. The velocity resolution for the overall system was measured to be 4% for $Z = 1$ and $\beta \simeq 1$ particles. The charged particle trigger is provided by the match between all four ToF layers [20]. Charge resolution of ToF according to the measurements is $\delta Z \simeq 0.05$ for a $Z = 1$ particle [14].

3.1.1.6 Electromagnetic Calorimeter

Charged particles deposit energy in their interactions with materials and especially rapidly lose energy in dense materials. This phenomenon measured in a dedicated calorimeter is called a particle shower. By using a fine granularity calorimeter, the profile of the energy deposited can be measured and the type of the particle determined.

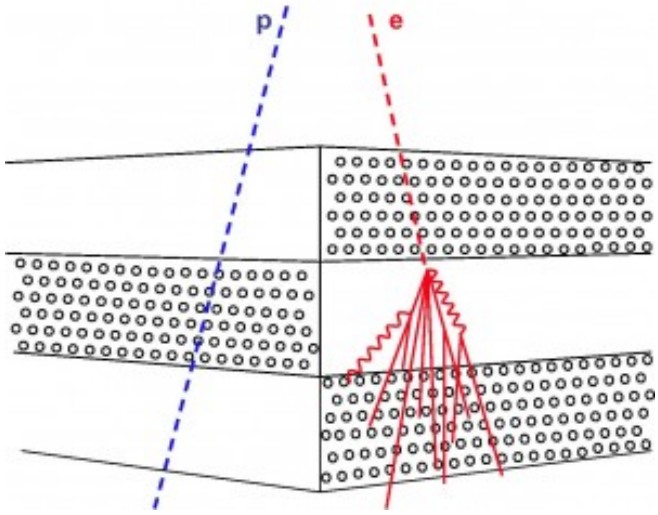

Figure 3.4: The different reactions in ECAL when an electron and a proton passes through [48].

The characteristic length of interaction for an electromagnetic interaction is radiation length, details of which are given in Chapter 2. An electromagnetic calorimeter generally has more than a couple of radiation lengths. The amount of radiation lengths in a calorimeter depends on factors such as the cost and the size of the calorimeter [51]. Since the shower length increases logarithmically with increasing energy, the

thickness of the detector to fully measure the shower should increase logarithmically with the energy of particles. The amount of shower which is not contained inside the active area of the calorimeter is defined as the leakage. Leakage leads to lack of information regarding the particle since the overall shower information is not acquired. The thickness of the calorimeter which includes the $95\ \%$ of the total shower energy is calculated as:

$$t_{95\ \%} \simeq t_{max} + 0.08Z + 9.6 \tag{3.5}$$

where unit for $t_{95\ \%}$ and t_{max} is in radiation lengths and Z stands for the atomic number of the material. In a calorimeter with $X_0 \simeq 25$, the leakage in longitudinal direction is less than $1\ \%$ for electrons with energies up to $300\ GeV$ [35].

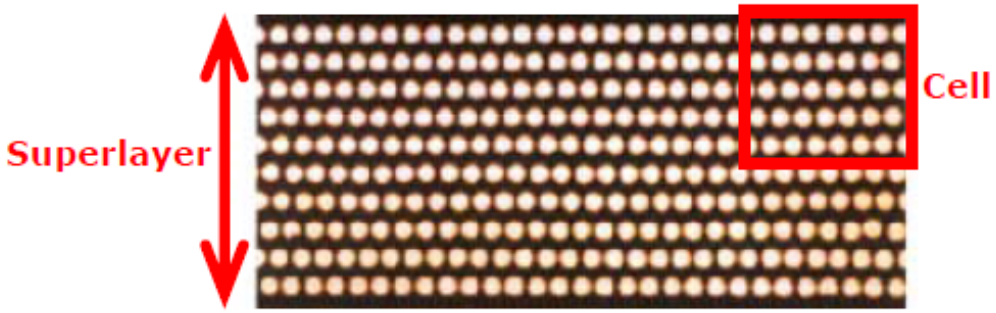

Figure 3.5: A part of the lead-fibre-glue composite structure of the ECAL [49].

The AMS-02 ECAL is designed for discriminating $e^{\pm}$ and photons which interact electromagnetically from the more abundant protons which interact hadronically. Since the charges of a positron and a proton are the same, the only subdetector capable of discriminating them is ECAL in addition to TRD. ECAL can discriminate one positron in about 10^5 protons. The total depth of the instrument is equal to 17 radiation lengths and also to 0.6 nuclear interaction lengths [49]. Electrons shower electromagnetically and they can deposit all of their energy in the calorimeter while at high energies, the shower may not be fully contained and might leak outside the calorimeter. A hadronically showering particle such as proton has a lower probability of showering inside the ECAL since 0.6 nuclear interaction length is not enough to stop it. If these protons were to act as minimum ionizing particles (MIPs), then they would leave an energy deposition of about $2.1\ GeV$ in the calorimeter. Therefore, this analysis is carried out above $5\ GeV$ in order to reject the considerable amount of low energy protons trapped in the geomagnetic field of the Earth. A figure showing

an electron and a proton passing through ECAL is shown in Figure 3.4.

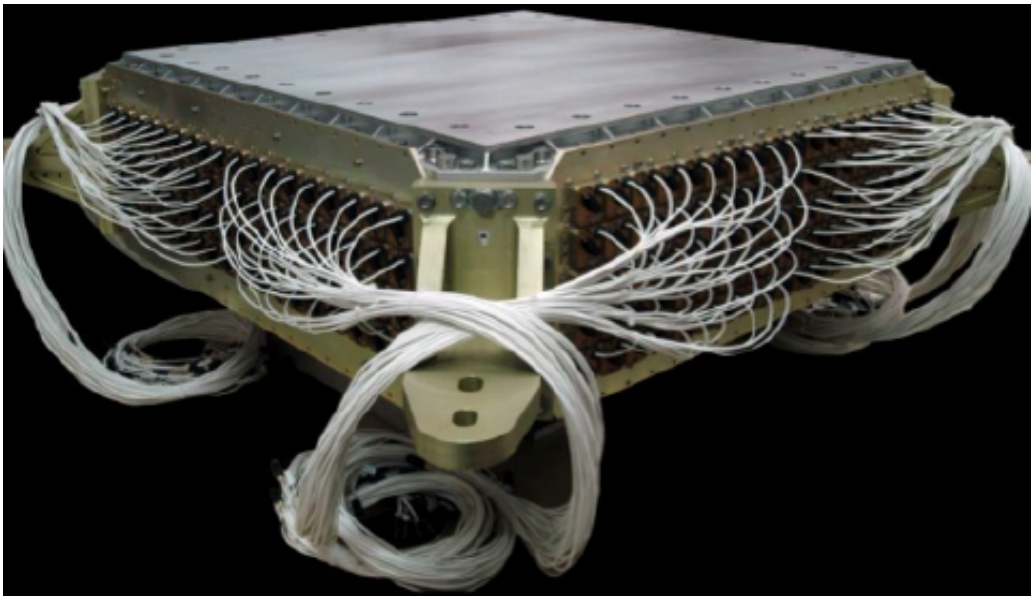

Figure 3.6: An image of the support structures and the fibres of the ECAL [49].

The AMS-02 ECAL is constructed out of lead/scintillating fibre sandwiches and it has an active volume of $648 \times 648 \times 166.5\ mm^3$ [49]. It is composed of $18.5\ mm$ thick superlayers. Each of them is made of eleven 1 mm thick lead foils which are grooved, interleaved with layers of 1 mm diameter scintillating fibres and then glued together with epoxy [49]. This structure is shown in Figure 3.5.

The resulting composite structure has a density of $6.8 g/cm^3$ and the active part of the ECAL has an approximate total weight of 638 kg. The main sensors of the ECAL are Hamamatsu R-7600-00-M4 multianode photomultipliers and the plexiglass light guides, which reduce the cross-talk and maximize the collection of light, couple to the fibres. Silicone joints enhance the optical contacts. Every PMT has $8.9 \times 8.9 mm^2$ anodes. There are 18 layers in longitudinal and 72 samplings in lateral direction which amounts to 1296 readout units in total. In order to achieve the 3-D imaging for the shower development, 10 layers, which is equivalent to 5 superlayers, are in $\hat{y}$ and 8 layers, which is equivalent to 4 superlayers, are in $\hat{x}$ direction. These superlayers alternate between these directions [55]. An image of the ECAL with the support structures and the fibres can be seen in Figure 3.6.

When a particle showers in the ECAL and after a high energy deposition occurs in the inner layers of the ECAL, a fast signal is created and processed by the trigger

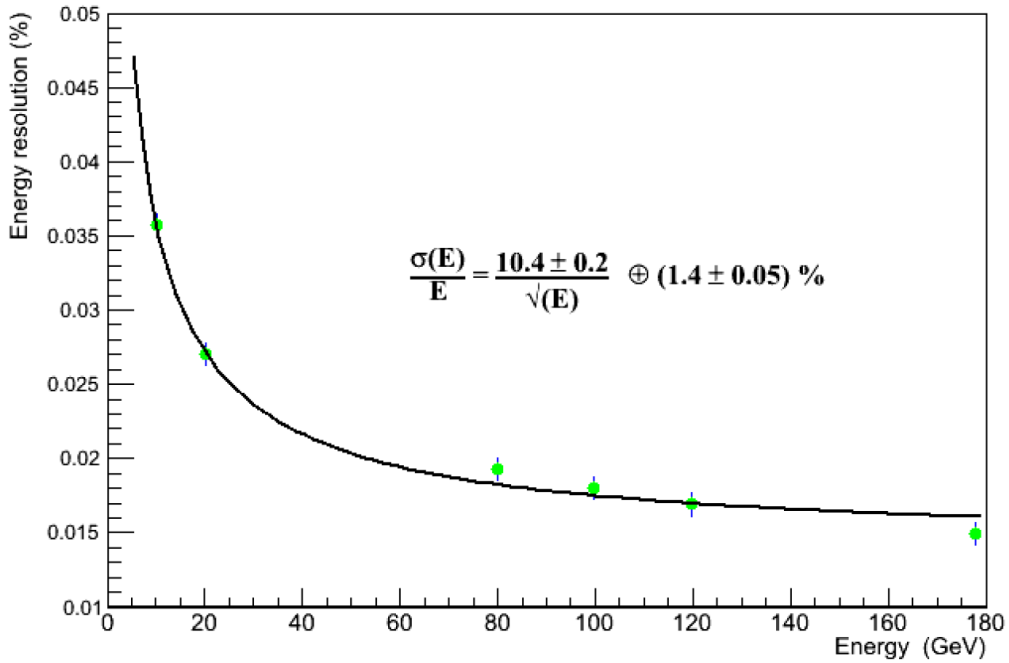

Figure 3.7: Energy resolution of the ECAL with respect to the energy of the test beam [55].

board that allows the acquisition of the event in 240 ns. An angular cut is used as an additional trigger for the discrimination of charged particles and photons that enter the ECAL from angles outside its field of view. For x and y projections separately, the direction of the incoming particle is calculated by finding the mean position of the PMTs which are fired. In order to select particles inside the AMS-02 geometrical acceptance, an angular cut of 20^o is applied. The expected unconverted photon trigger efficiency is 20 % at 1 GeV and is 99 % at 10 GeV. Photon trigger rates were calculated using the Monte Carlo simulations based on the data from AMS-01. Particles which fire the AMS-02 charged trigger including conversion mode photons are not included in this calculation [49].

AMS-02 detector was tested at Super Proton Synchrotron (SPS) at CERN with 400 GeV proton beam. In order to understand the performance, positron, electron and proton beams between 8 and 400 GeV were used. After equalizing each channel for getting the same response for the same energy deposit and correcting the energy depositions for leakages, the energy resolution is calculated. As shown in Figure 3.7, for energies above 50 GeV, the energy resolution is lower than 2% [55]. In the thesis on conversion mode photons by Emirhan Postacı, the energy resolution of the ECAL

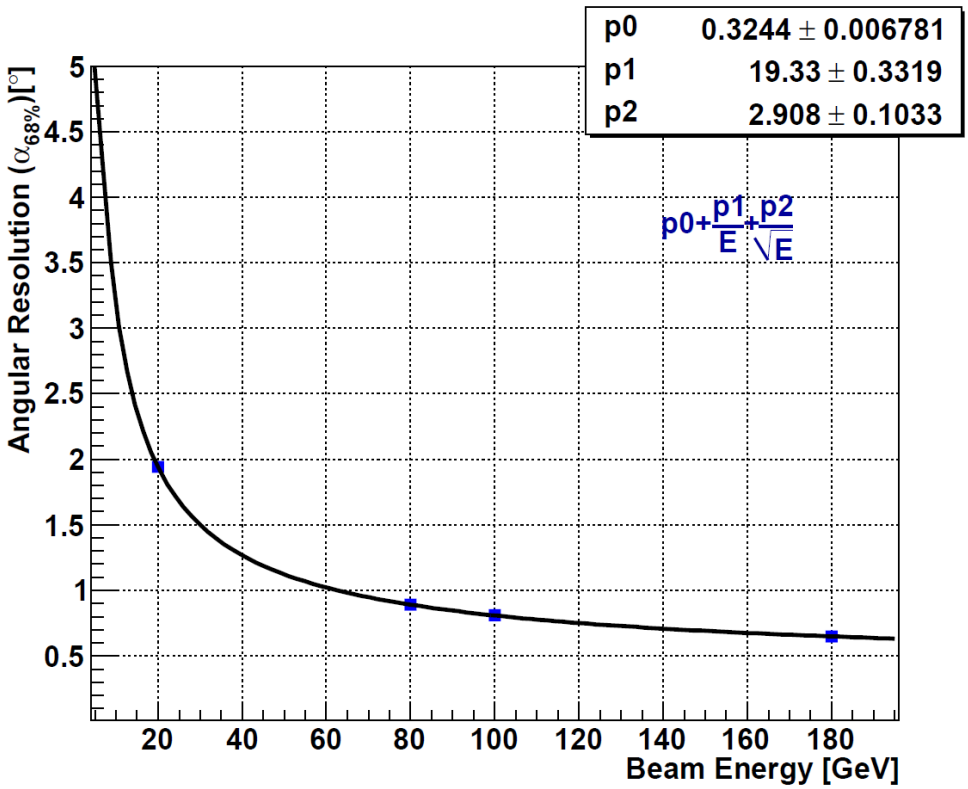

Figure 3.8: Angular resolution of the ECAL with respect to the energy of the test beam [55].

was calculated [44].

Another important aspect of ECAL is that it can measure the energy and the direction of high energy photons [48]. Since the cosmic origin of the photons is investigated, the angular resolution of the ECAL is extremely important for gamma ray physics. In this analysis, it is assumed that the electron and photon showers are similar, the angular resolution is calculated using the Test Beam of electrons. Figure 3.8, shows the angular resolution of the ECAL with respect to the test beam energy. Angular resolution at $50\ GeV$ is approximately $2\ \%$ [55]. An investigation of angular resolution of the ECAL was conducted by Emirhan Postacı [44].

3.2 Photon Analysis with AMS-02

The analysis of photons with AMS-02 has two modes depending on the initial interaction point of the particle. These modes are called conversion and calorimetric, and

will be discussed here.

3.2.1 Conversion Mode

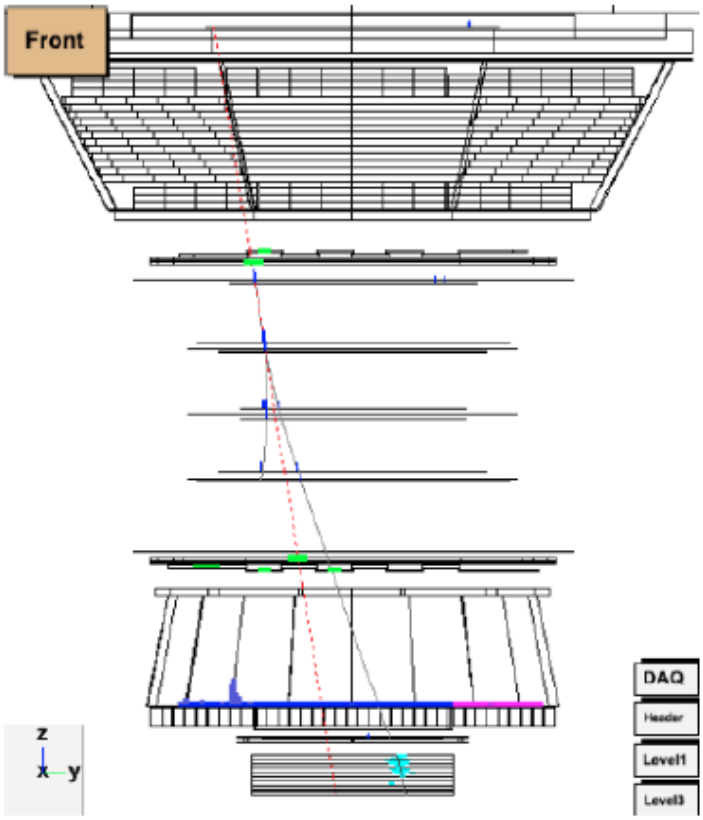

Figure 3.9: An example of a conversion mode photon from Monte Carlo simulations. The pair production occurs in the upper ToF layer and two particle tracks one for a e^+ (on the right) and one for an e^- (on the left) which are bent in different directions. The reconstructed axis for the incoming photon is shown with red dashed line. One of the particles showers in the ECAL and both of them give clusters in lower ToF as well. [30].

While all the detectors above the ECAL have been optimized to minimize multiple scattering, and while it has a low probability, photons can still pair produce in the material before reaching the ECAL. If a photon pair produces an electron-positron pair above upper ToF layers, then these particles can be reconstructed as two tracks and a vertex can also be reconstructed. The tracker can reconstruct e^+e^- pairs as two tracks below $50GeV$ but above this energy, the tracker can only resolve them as one

track due to limited spatial resolution, like the one shown in Figure 3.9. An analysis on high energy conversion mode photons was conducted using AMS-02 data [44] by Emirhan Postacı for high energies. However, no photon candidates were found [44].

3.2.2 Calorimetric Mode

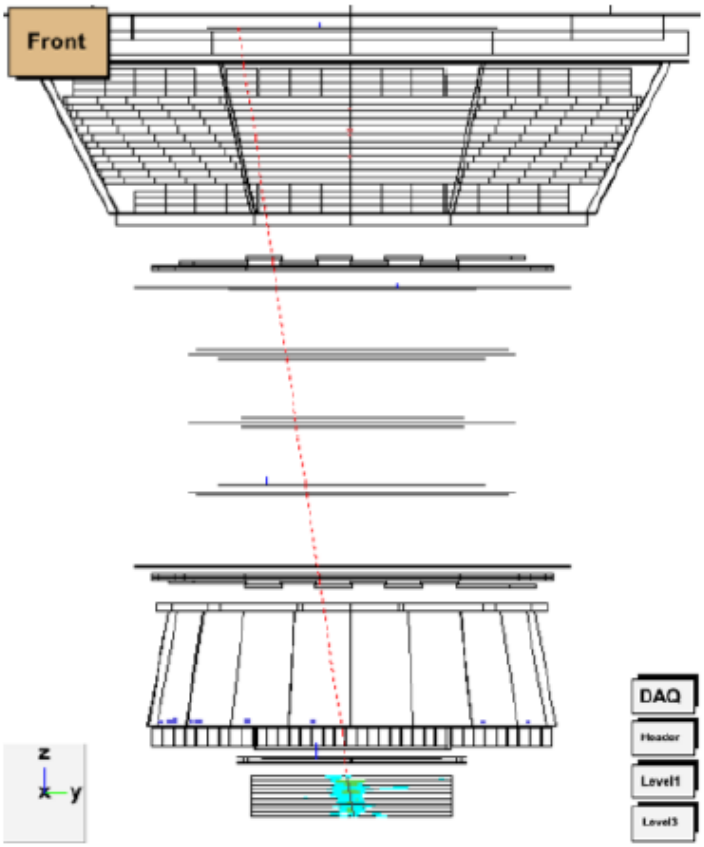

Figure 3.10: An example of a calorimetric mode photon from Monte Carlo simulations which interacts with non of the sub detectors except for the ECAL. The photon starts showering after entering the ECAL. The red dashed line indicates the shower axis. Hits in the tracker and the RICH are due to the back-scattered particles coming from the ECAL. [30].

The ECAL has the highest radiation length when compared to other subdetectors in AMS-02. The photons which go through the upper sub detectors without interacting may enter the ECAL and then pair produce. These photons are called calorimetric photons and they are the topic of this analysis and the analysis will be detailed in Chapter 4. An example event of this type is shown in Figure 3.10.

3.3 Publications of AMS-02

The AMS-02 has published four papers and seven proceedings. Two of these papers include positron fraction in different energy intervals. Third publication is about the individual fluxes of positron and electron. They will be discussed here briefly.

High Statistics Measurement of the Positron Fraction in Primary Cosmic Rays of $0.5 - 500GeV$ ***with the Alpha Magnetic Spectrometer on the International Space Station***

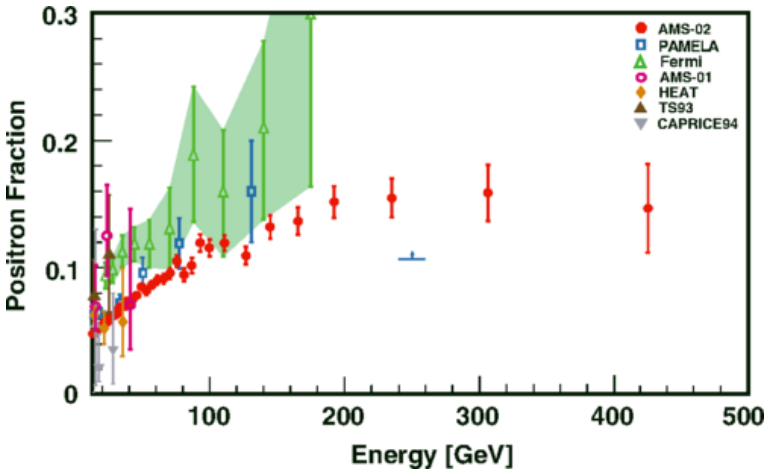

Figure 3.11: The second publication of the AMS-02 collaboration which shows the positron fraction with respect to the reconstructed energy which is extended to $500\ GeV$ and compares the result with the results of PAMELA [10] and the FERMI-LAT [6] experiments. [5]

On April 5, 2013, the first publication of AMS-02 on the positron fraction was published. This publication covered the energy range between $0.5 - 350\ GeV$ [14]. The second publication, again on the positron fraction, extends energy range of the first results of the AMS-02 experiment from $350\ GeV$ to $500\ GeV$ and increases the precision with more statistics. Between the energy range $0.5 - 500\ GeV$, 10.9 million positron and electron events are presented. Figure 3.11 shows the positron fraction above $10\ GeV$. Above this energy, the fraction starts increasing and this behaviour goes until about $200\ GeV$. However, above $200\ GeV$, the fraction does not increase any more. The comparisons from other experiments such as PAMELA [10] and FERMI-LAT [6] are also shown in the plot.

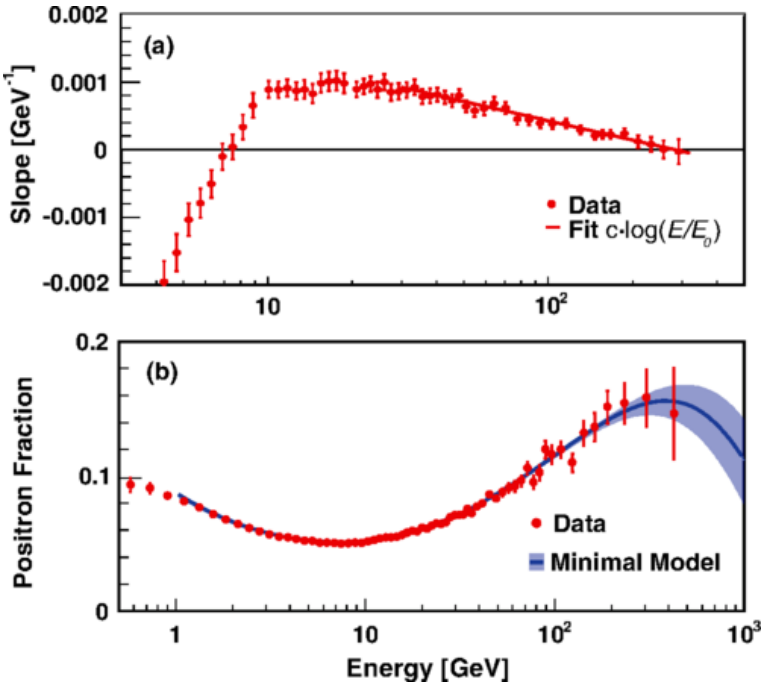

Figure 3.12: (a) This figure shows the slope for the positron fraction with respect to the energy. It shows the slope for the whole energy range except for below $4\ GeV$ which is off scale. The line was calculated from a logarithmic fit to the data for above $30\ GeV$. (b) Solid curve shows the fit of a minimal model to the positron fraction and the shaded area shows $68\ \%$ C.L. range for the parameters of the fit. [5]

Electron and Positron Fluxes in Primary Cosmic Rays Measured with the Alpha Magnetic Spectrometer on the International Space Station

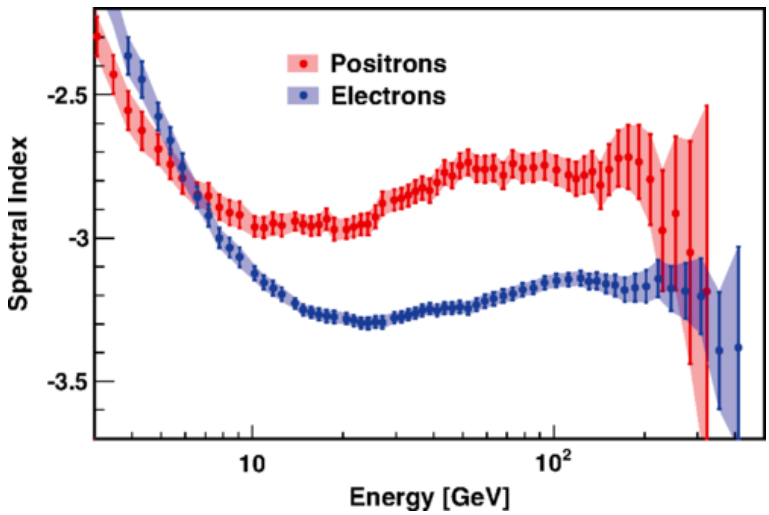

Figure 3.13: Spectral indices for the positron and electron fluxes with respect to reconstructed energy [12]

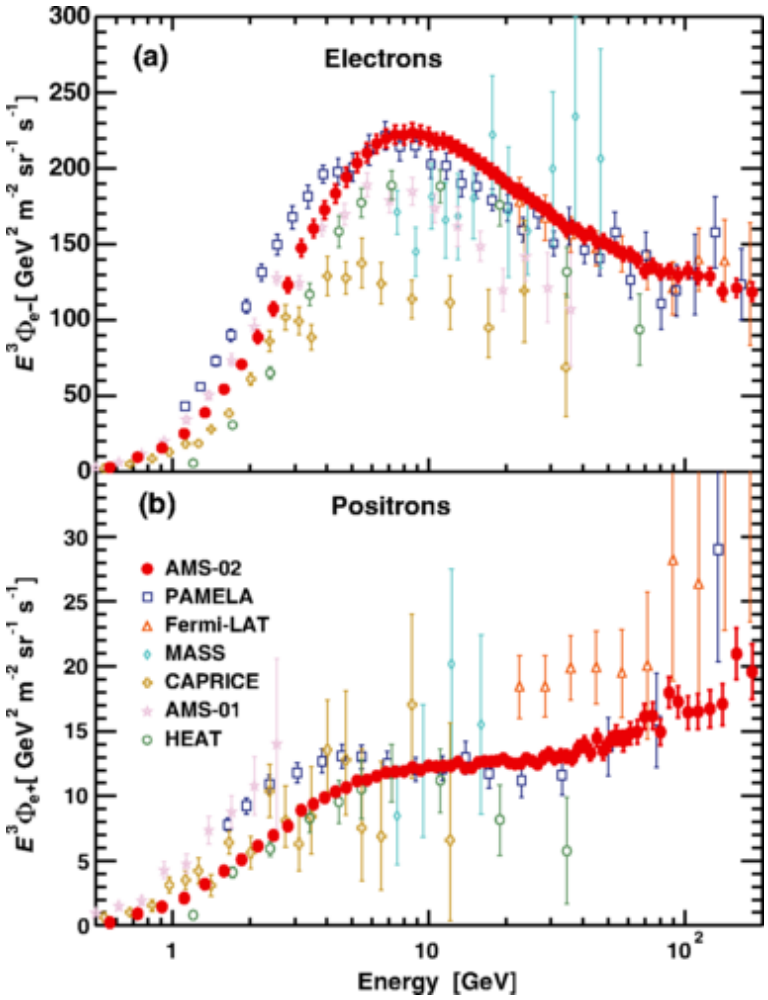

Figure 3.14: Fluxes for the (a) electron and (b) positron multiplied by E^3 with respect to reconstructed energy for the energies below $200\ GeV$. Comparisons with the results of PAMELA [10], Fermi-LAT [6], MASS [36], CAPRICE [21], AMS-01 [11] and HEAT [33] are also shown. [12]

Third publication is on the separate fluxes of electrons and positrons. For electrons, energy range between $0.5 - 700\ GeV$ and for positrons, energy range between $0.5 - 500\ GeV$ are presented. The power law spectrum for both of the fluxes require an explanation beyond a single power law spectrum. The energy dependence and the magnitude are different for each of the fluxes both of which change their behaviour at about $30\ GeV$. For the energy range between $20 - 200\ GeV$, the spectral index for positrons is dramatically harder than the one for the electrons as shown in Figure 3.13.

Figure 3.14 shows the positron and electron fluxes with respect to energy. The plots

indicate that the behaviour of the two fluxes are different than each other they both change behaviour with the increasing energy. Figure 3.15 shows the fluxes for the total energy range. The behaviour of both of the fluxes is different in the high energies as well as low energies.

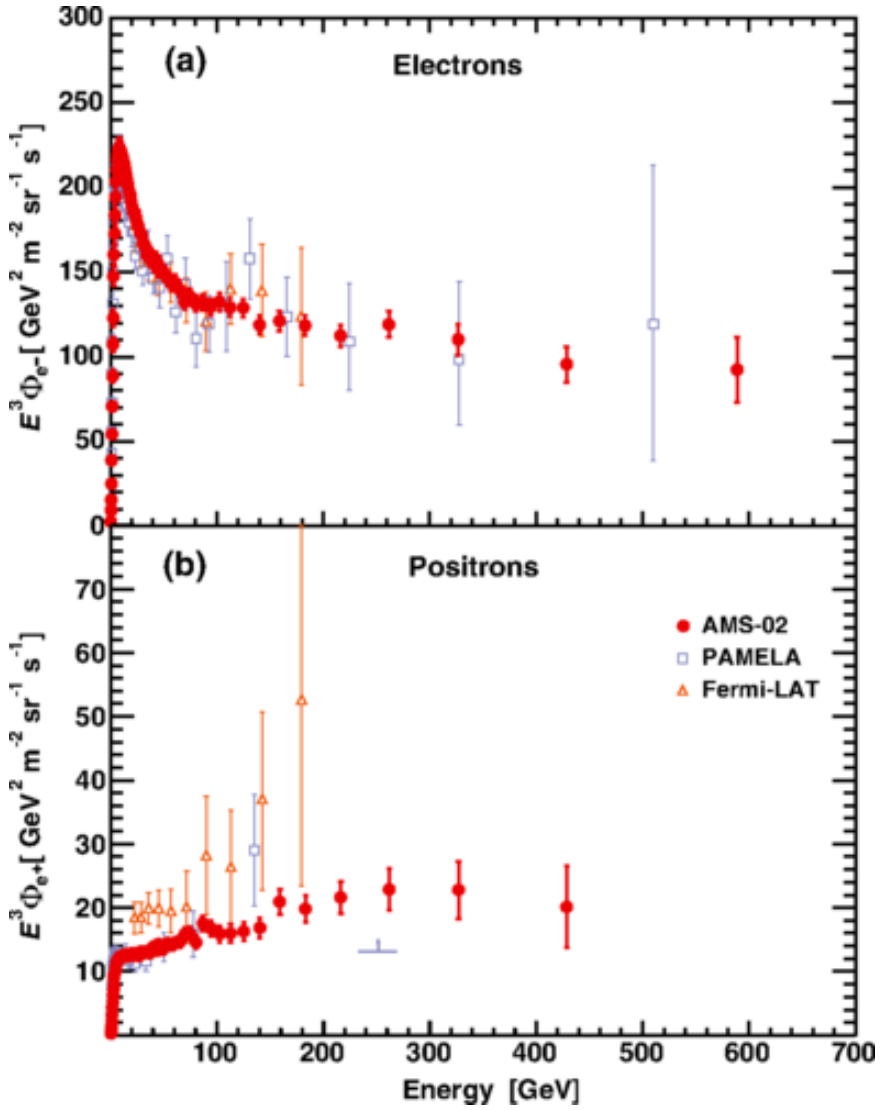

Figure 3.15: Fluxes for the (a) electron and (b) positron multiplied by E^3 with respect to reconstructed energy for the whole energy range. Comparisons with the results of PAMELA [10] and Fermi-LAT [6] are also shown. [12]

Precision Measurement of the $e^+ + e^-$ Flux in Primary Cosmic Rays from 0.5 GeV to 1 TeV with the Alpha Magnetic Spectrometer on the International Space Station

In the third publication of AMS-02, separate fluxes of positrons and electrons were investigated up to 500 GeV and 700 GeV, respectively. In the fourth publication, com-

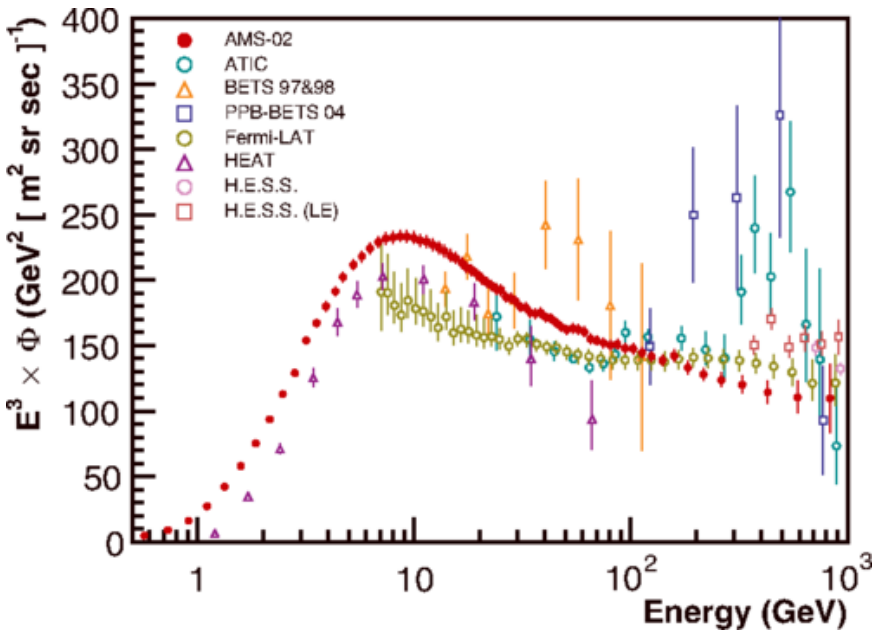

Figure 3.16: Fluxes for the combination of positrons and electrons multiplied by E^3 with respect to reconstructed energy for the whole energy range. Error bars include both statistical and systematic errors [13]. Comparisons with the results of earlier experiments are also shown. [54, 34, 26, 57, 15, 16, 7]

bined flux of positrons and electrons were investigated in the energy range between $0.5\ GeV$ and $1\ TeV$. The analysis includes 10.6 million positron and electron events in total. The flux above $30.2\ GeV$ can be explained using a single power law which has a spectral index as $\gamma = -3.170 \pm 0.008(stat + syst) \pm 0.008$ (energy scale). In Figure 3.16, the flux for the whole energy range is shown [13].

CHAPTER 4

CALORIMETRIC MODE PHOTON ANALYSIS

In this chapter, calorimetric mode photon analysis for energies above 5 GeV will be presented. The analysis includes photons which convert to electron-positron pairs after entering ECAL. ECAL is the main detector used in this analysis. Other sub detectors are only used as veto for other particles like protons, electrons and helium as well as photons which convert before entering the ECAL. This is a cut based analysis in which different variables from each sub detector is used to differentiate between photons and other particles. The dominant background for this analysis is the protons which are abundant in space. Both energy and angle information are retrieved from the ECAL. After the details of the analysis is presented, the physics results will be discussed.

4.1 Event Selection

4.1.1 Measurement of Variables Using Monte Carlo Simulations and Data

For understanding the differences between photons and their major background protons, Monte Carlo samples which include photons which are created from a square plane $35\ cm$ above AMS-02 and protons which are created from the same plane and also from the cube surrounding AMS-02 with energies between 5 and 2000 GeV were used. For the analysis, data taken with AMS-02 from May 19th, 2011 and February 28th, 2014 is used.

Binning

In this analysis, most of the variables which we use for the selection of the events are drawn with respect to the reconstructed energy which was retrieved from the ECAL. Binning used for the reconstructed energy is from 0.25 to 2000 GeV and it increases logarithmically in 60 bins. The reason for using this binning is to see the power law behaviour of the energy spectrum.

Data Quality Selection

In order to use the best data available, the commissioning data which was not calibrated is not used in this analysis. This data was eliminated using the "bad run cut" available in AMS-02 software. In addition, the data which has hardware errors was not used as well.

The events taken during AMS-02's passage through the South Atlantic Anomaly region has a high occupancy of simultaneous particles entering AMS-02 The SAA is caused by the shift of the Earth's axis of magnetic dipole field. This shift leads trapped low energy particles to become closer to the Earth's surface [29]. In order to eliminate these events, the live time of the trigger system is required to be greater than 0.5. Since the magnetic flux in South and North poles is more dense than other parts of the Earth, there is a high particle occupancy. Since this phenomenon contaminates the detector, these events should be eliminated. The average number of TRD hits per event are required to be less than 1000.

As the ISS travels around the Earth, it changes its orientation from time to time and the $\hat{z}$ of the AMS-02 can point to the Earth or the horizon. Since only the photons coming from the cosmos are desired for the analysis, this data should not be used. In order to achieve this, Zenith angle of ISS is required to be above 40^o.

Preselection

Since the analysis is based on photons interacting after entering the ECAL, one and only one particle shower in the ECAL is required. In order to guarantee the shower of the photons to start after entering ECAL and not before, a calorimetric cut requiring no interaction in the coordinates above the ECAL is used for the photon Monte Carlo.

The axis of the particle shower in the ECAL is reconstructed considering the lateral energy deposition dispersion of the shower. This axis is called the ECAL axis. In order to make sure that particle goes through all of the subdetectors without leaving a signal before coming to the ECAL, ECAL axis is required to pass through the upper ToF layers. In this way, charged particles are vetoed efficiently.

If a particle enters the ECAL from below and showers the shower might be fully contained, and would not have any signal in the detectors above the ECAL, satisfying the previous condition. To eliminate this possibility, the particle shower is required to be down going.

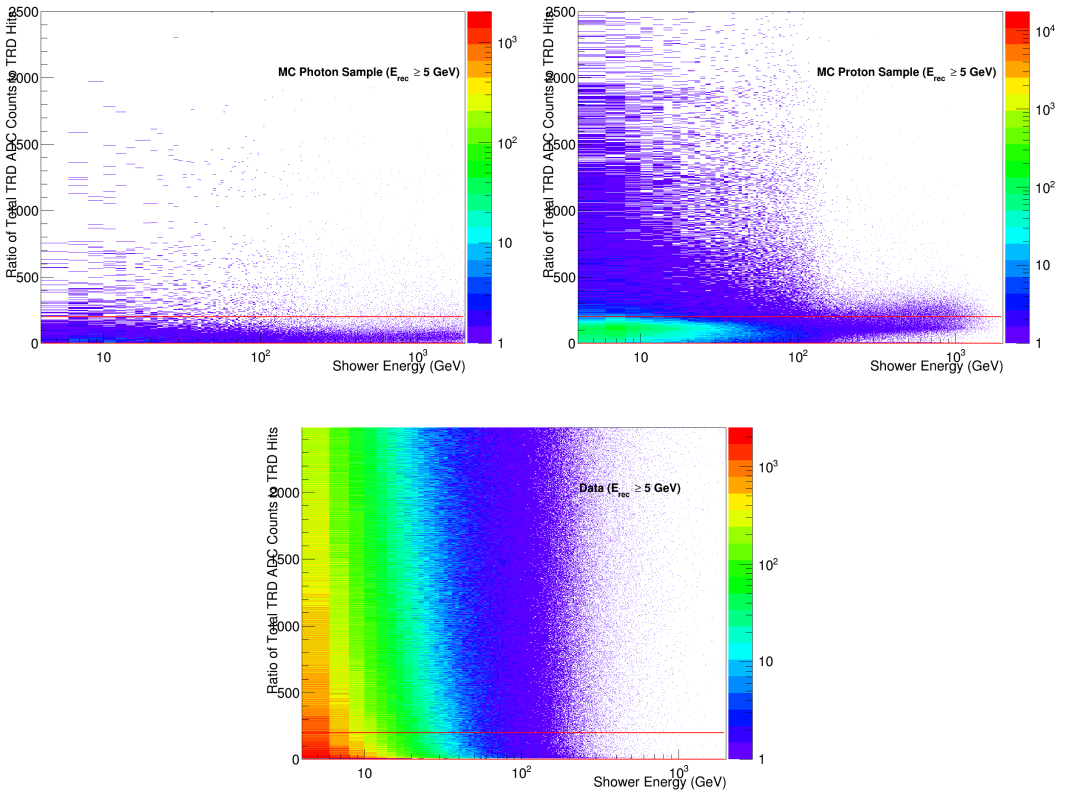

Figure 4.1: Reconstructed shower energy versus the sum of ADC counts for photon Monte Carlo (top left), proton Monte Carlo (top right) and data (bottom). The red line indicates the applied cut on this variable calculated as shown in Equation 4.1 and the events above this red line are discarded.

To ensure that the shower is well-reconstructed, the entrance and exit points of the shower are required to be two cells away from the edges of the ECAL. This cut is the fiducial volume cut. As the shower progresses downwards, it may not be fully

contained inside the ECAL volume. However, if the leakage is more than the reconstructed energy inside the ECAL, shower energy resolution suffers and these events are eliminated with the catastrophic leakage cut.

Since protons and helium nuclei behave may as MIPs depositing $2.1\,GeV$ and $8.4\,GeV$, the events below $5\,GeV$ are cut to reduce their background.

In the upcoming sub sections, where each cut will be discussed in detail, histograms are drawn with respect to the reconstructed energy for photon Monte Carlo, the dominant background proton Monte Carlo and data. If a proton often coming from the sides of the TRD is not reconstructed as a track in the Tracker or the TRD and scatters to pions inside AMS-02 which then showers in the ECAL, this can look similar to the signal events that are investigated in this analysis.

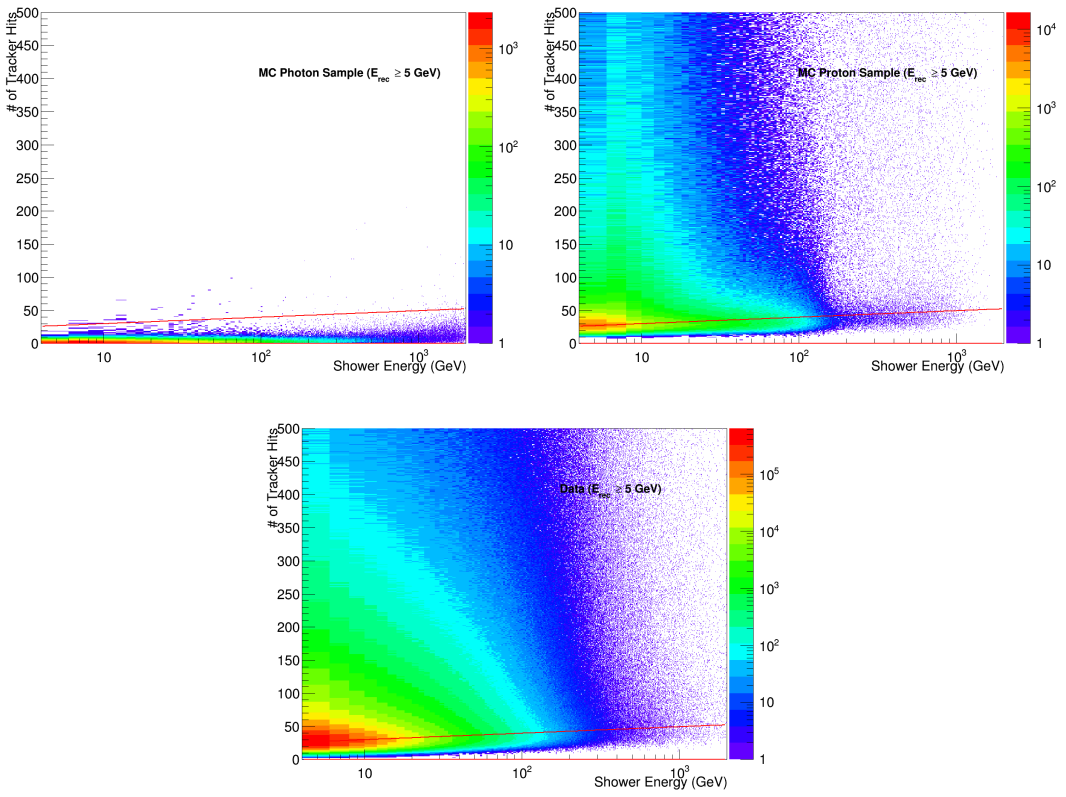

Figure 4.2: Reconstructed shower energy versus number of tracker hits for photon Monte Carlo (top left), proton Monte Carlo (top right) and data (bottom). The red line indicates the applied cut on this variable calculated as shown in Equation 4.2 and the events above this red line are discarded.

TRD Cuts

TRD cuts are useful for eliminating electrons and positrons. Tracks of particles entering AMS-02 TRD simultaneously with a photon can be reconstructed in TRD If these events, which have less than 3 TRD tracks, are eliminated, than a huge amount of photon events may be discarded as well. In order to keep most of the photons, events which have more than 3 TRD tracks are eliminated while the events which have less than 3 TRD tracks are eliminated only if any of them points toward the ECAL. Generally, these particles would confuse the photon reconsctruction, but if they are not pointing towards the ECAL, they can be safely retained.

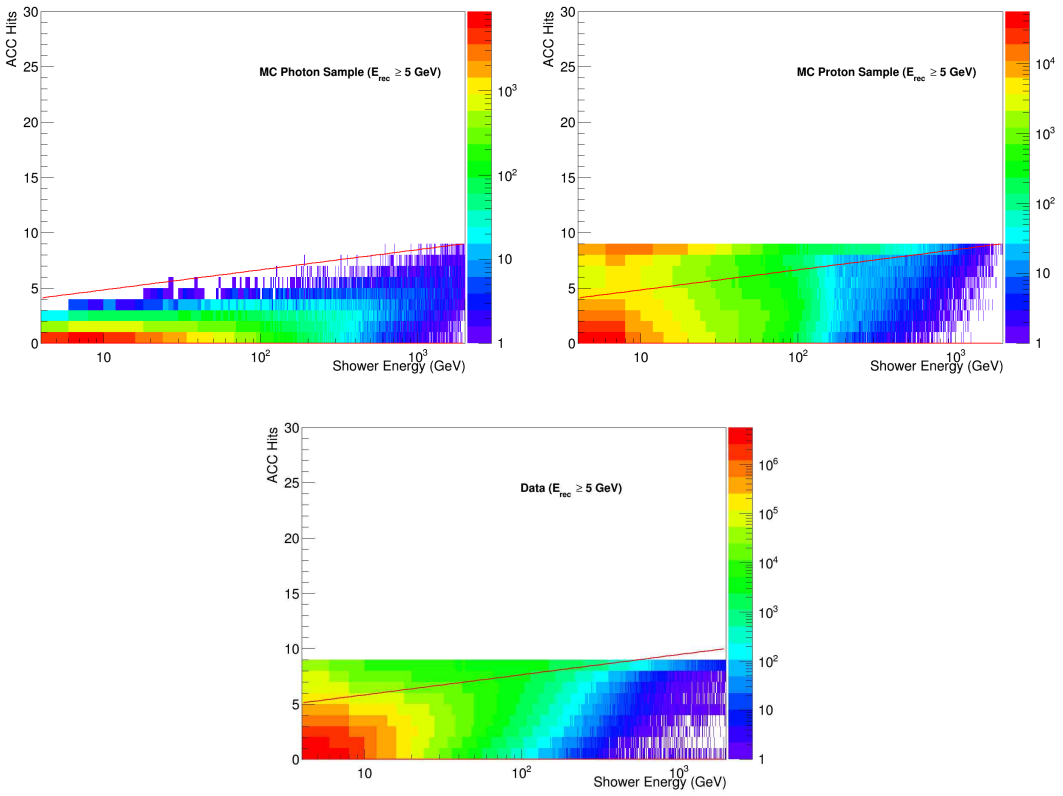

Figure 4.3: Reconstructed shower energy versus number of ACC hits for photon Monte Carlo (top left), proton Monte Carlo (top right) and data (bottom). The red line indicates the applied cut on this variable calculated as shown in Equation 4.3 and the events above this red line are discarded.

Another cut to reduce the significant proton background is, an energy based cut on ratio of the total number of ADC counts to the hits in the TRD. Rarely the back scattered particles from interacting in the ECAL will reach the TRD and leave small

amounts of energy depositions in the TRD, reflected in the ratio of total number of ADC counts to the hits. This parameter is used to differentiate between protons, which do not give out transition radiation at low energies, from the back scattered positrons and electrons of the ECAL photons. The cut applied on this parameter is as follows:

$$\text{Total Number of ADC Counts / Number of Hits} = 200.0 \quad (n.u.) \tag{4.1}$$

This effect and the employed cut is shown in Figure 4.1 on the histograms drawn for photon and proton Monte Carlo simulations and data, with respect to the reconstructed ECAL energy.

Tracker Cuts

Conversions above the ECAL are not desired in this analysis and a cut on the tracker tracks and the number of hits can eliminate the conversions before the tracker and the charged particle background.

However, back scattered particles from the particle showers in the ECAL also leave hits in the Tracker. The number of tracker hits left by the calorimetric photons and protons are different based on the energy of the particles as seen in Figure 4.2. Number of tracker hits is an important variable for eliminating charged particles which were not reconstructed as tracks.

$$\text{Number of Tracker Hits} = 20.00 + 9.79 \cdot log_{10}(E_{rec}) \quad (n.u.) \tag{4.2}$$

ACC Cuts

The number of ACC hits indicate particles coming from the sides of AMS-02. For the calorimetric mode photon analysis, an energy based cut is used as shown in the Figure 4.3. Particles coming from the sides are mostly eliminated while preserving particles that are back scattered from the ECAL. The equation used for this cut is as follows:

$$\text{Number of ACC Hits} = 3.00 + 1.82 \cdot log_{10}(E_{rec}) \quad (n.u.) \tag{4.3}$$

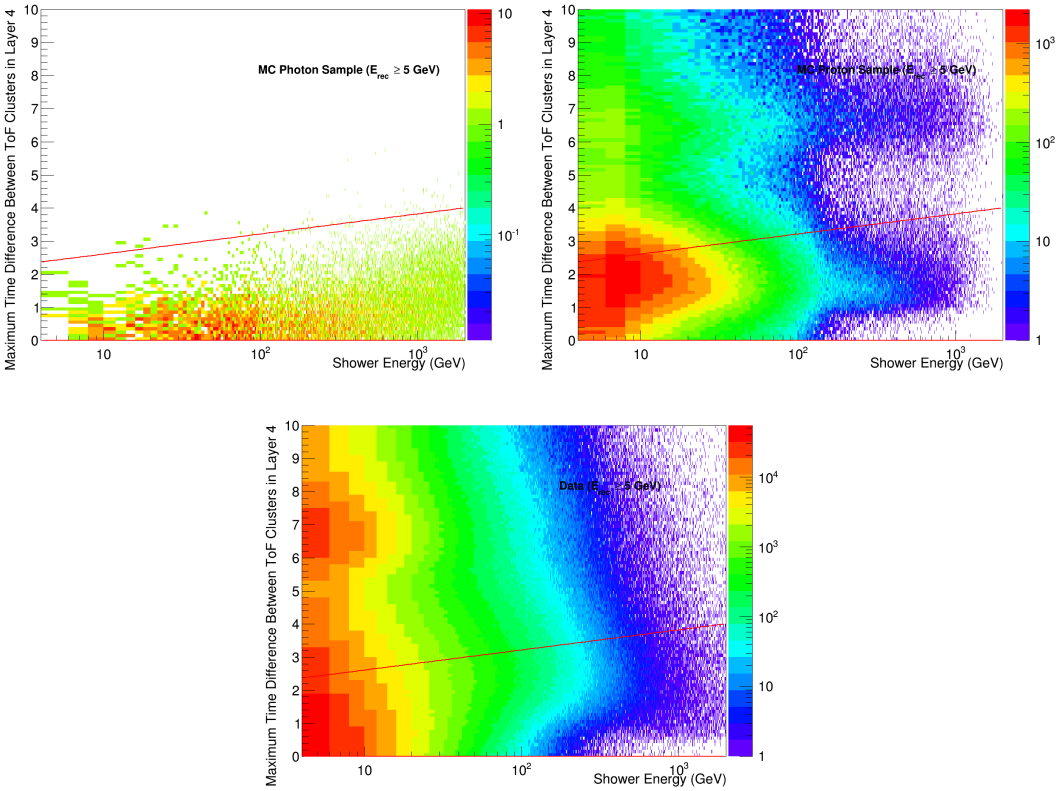

Figure 4.4: Reconstructed shower energy versus maximum time difference between clusters in Layer 4 for photon Monte Carlo (top left), proton Monte Carlo (top right) and data (bottom). The red line indicates the applied cut on this variable calculated as shown in Equation 4.4 and the events above this red line are discarded.

ToF Cuts

Since the photon conversions above the ECAL are not desired in this analysis, particles which are identified as downgoing by the Time of Flight detector are eliminated. However, back scattered $e^{\pm}$ from ECAL photons also leave signals in ToF. By using the ToF timing, the background particles which are not reconstructed as tracks in TRD and Tracker can be discarded. For this reason, clusters in Layer 1 and Layer 4 are taken into account. Having a cut on Layer 4 only helps with the elimination of the charged particles which do not leave a track in TRD and Tracker as well as clusters in ToF Layer 1 or 2.

However, if a downgoing charged particle goes through ToF Layer 1 or 2 without generating a cluster and deposits a cluster in Layer 4, and its backscatter generates

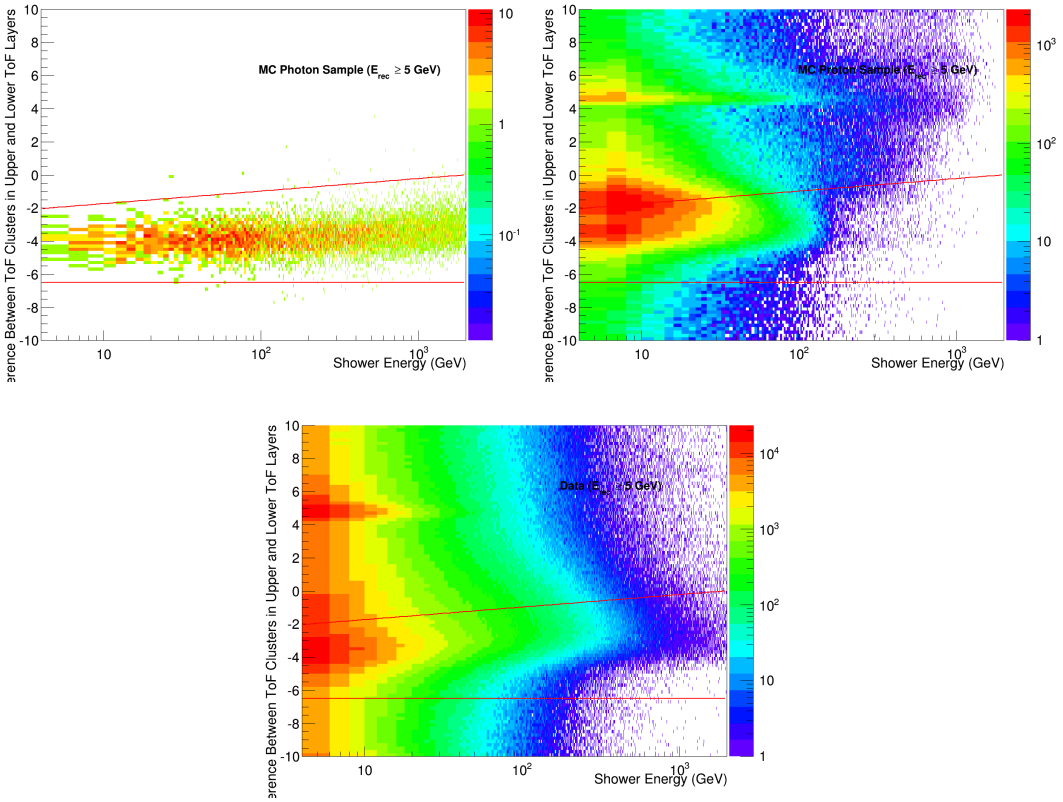

Figure 4.5: Reconstructed shower energy versus maximum time difference between clusters in Layer 1 and Layer 4 for photon Monte Carlo (top left), proton Monte Carlo (top right) and data (bottom). The red lines indicate the applied cuts on this variable calculated as shown in Equation 4.5 and the events outside these red lines are discarded.

another cluster in ToF Layer 4, it can be distinguished from the two back scattered particles coming from an ECAL photon. In Figure 4.4, the maximum time difference between clusters in Layer 4 with respect to reconstructed shower energy are shown for photon Monte Carlo, proton Monte Carlo and data. With a cut on this variable, these background events are discarded. The equation for this cut is:

$$\text{Max Time Diff. Between Clusters in Layer 4} = 2.00$$

$$+ 0.61 \cdot log_{10}(E_{rec}) \quad (ns) \tag{4.4}$$

If a charged particle goes through both upper and lower ToF layers and generate clusters in these layers, the maximum time difference between clusters in Layer 1 and Layer 4 for these events is different for the back scattered positrons and electrons

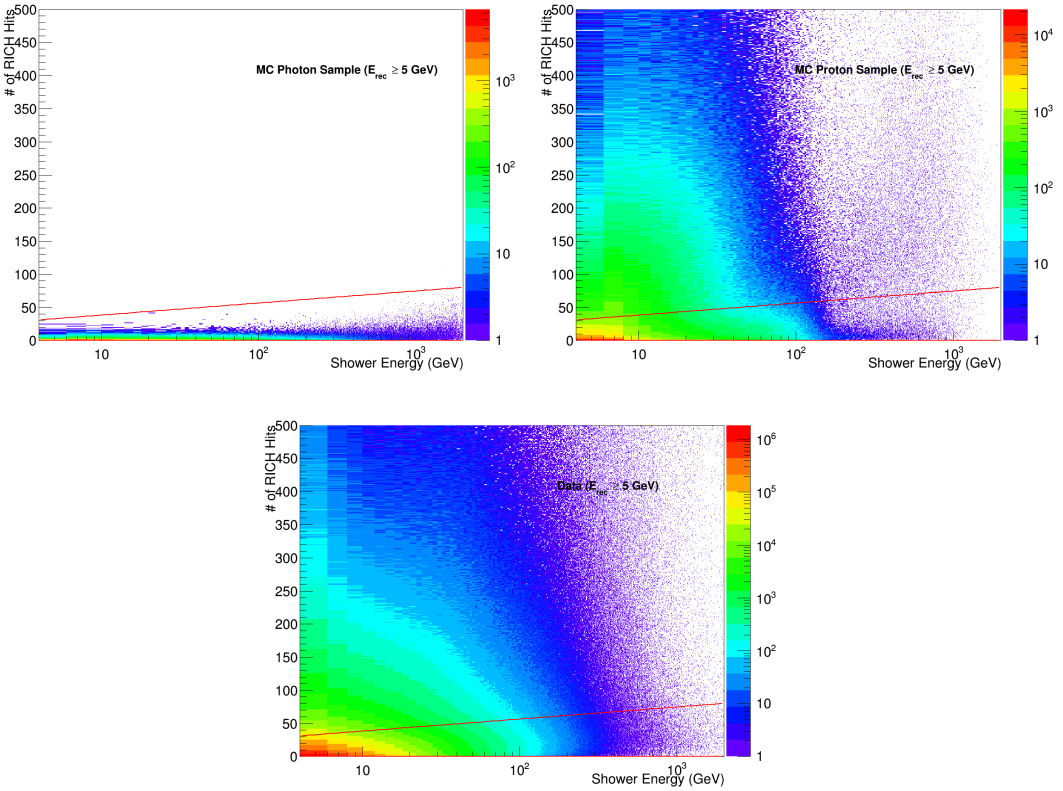

Figure 4.6: Reconstructed shower energy versus number of RICH hits for photon Monte Carlo (top left), proton Monte Carlo (top right) and data (bottom). The red line indicates the applied cut on this variable calculated as shown in Equation 4.6 and the events above this red line are discarded.

from the converted ECAL photons. As can be seen in the Figure 4.5, a cut on this variable is useful for eliminating charged particles without reconstructed TRD and Tracker tracks. The equations showing the applied cuts are:

$$-6.5 < \text{Max Time Diff. Between Clusters in Layer 1 and 4}$$

$$< -2.50 + 0.76 \cdot log_{10}(E_{rec}) \quad (ns) \tag{4.5}$$

RICH Cuts

Using the RICH information is another way to get rid of the charged particle background. Only downgoing charged particles create RICH rings in the detector, which are then reconstructed very rarely accidentals from back scattered particles form a photon ECAL shower can also be reconstructed as a RICH ring. A cut on RICH rings

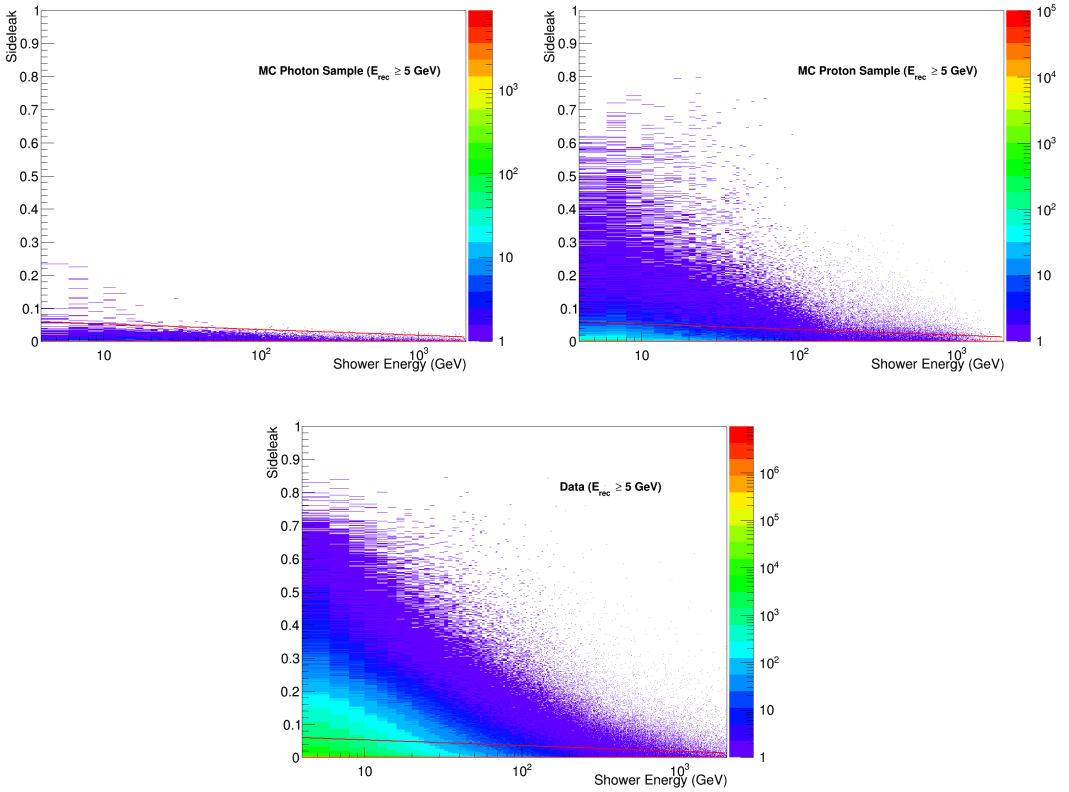

Figure 4.7: Reconstructed shower energy versus side leak for photon Monte Carlo (top left), proton Monte Carlo (top right) and data (bottom). The red line indicates the applied cut on this variable calculated as shown in Equation 4.7 and the events above this red line are discarded.

is employed without losing many photons. Another variable that is used is the number of RICH hits. The number of RICH hits differ for charged particles which goes through the RICH without generating a ring and for the back scattered particles from converted ECAL photons as can be seen in Figure 4.6. An energy based cut as

$$\text{Number of RICH Hits} = 20.00 + 18.18 \cdot log_{10}(E_{rec}) \quad (n.u.) \tag{4.6}$$

is shown in Figure 4.6 and it is useful to eliminate such events.

ECAL Cuts

ECAL cuts are applied after cuts in other subdetectors are applied For the selection, several different ECAL variables are used.

Side leak is a parameter which gives the leakage of the particle showers from the sides. Since hadronic showers are wider than electromagnetic showers, the leakage

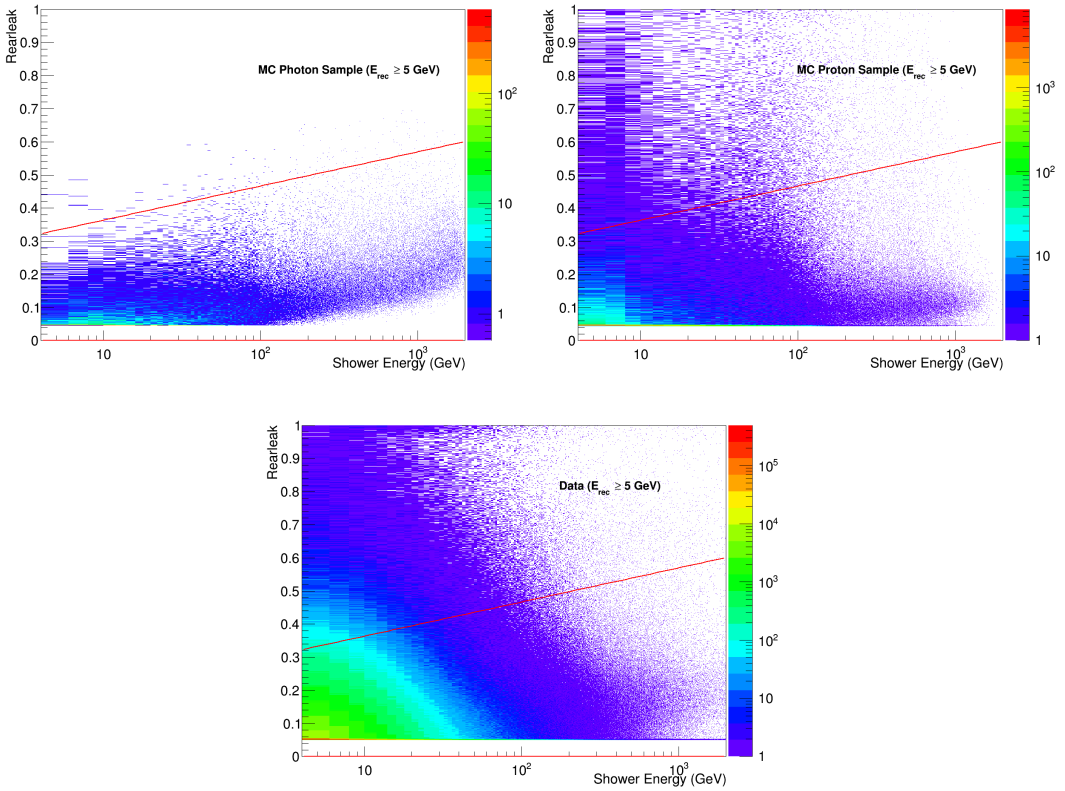

Figure 4.8: Reconstructed shower energy versus rear leak for photon Monte Carlo (top left), proton Monte Carlo (top right) and data (bottom). The red line indicates the applied cut on this variable calculated as shown in Equation 4.8 and the events above this red line are discarded.

from the sides is larger for protons and ions. As can be seen in the Figure 4.7, a cut on this variable is useful for eliminating protons and the function related to this cut is as follows:

$$\text{Side Leak} = 0.07 - 0.02 \cdot log_{10}(E_{rec}) \quad (n.u.) \tag{4.7}$$

Rear leak parameter gives the estimated leakage of the uncontained shower from the bottom of the ECAL. Stopping a hadronic particle is more difficult than stopping an electromagnetic particle which generally implies that protons will have a larger rear leak. Figure 4.8 shows this parameter for photon Monte Carlo, proton Monte Carlo and data with respect to the reconstructed ECAL shower energy. An energy based cut on this variable according to the equation

$$\text{Rear Leak} = 0.26 + 0.10 \cdot log_{10}(E_{rec}) \quad (n.u.) \tag{4.8}$$

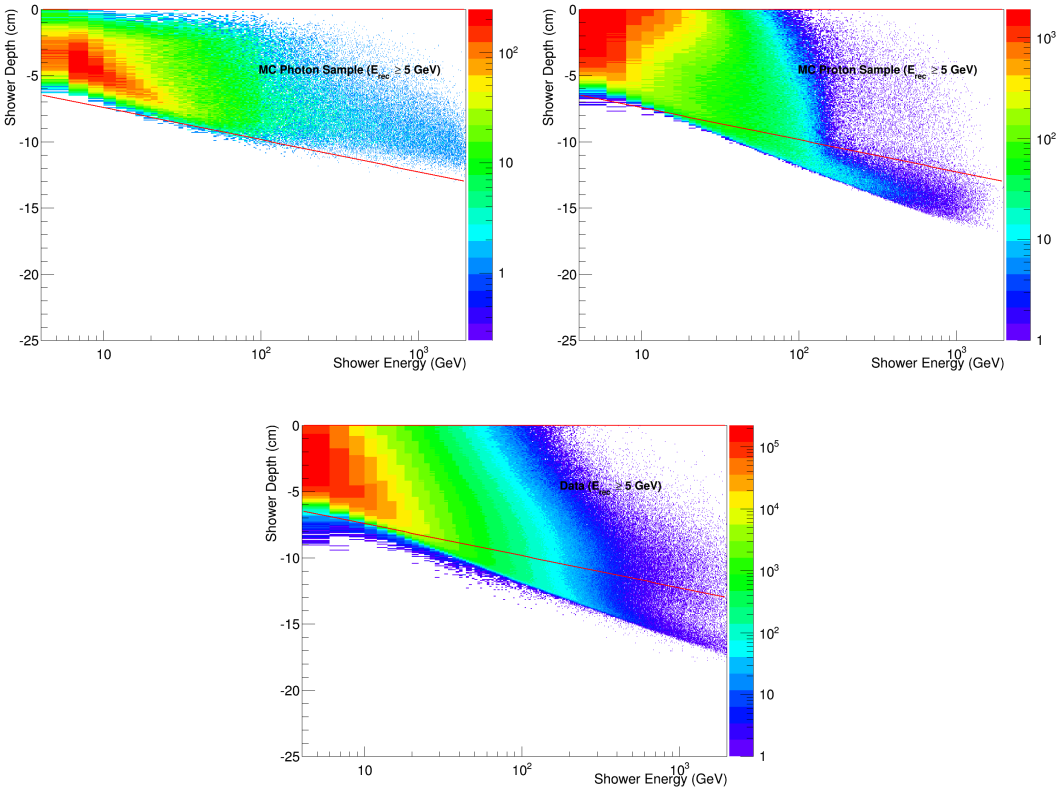

Figure 4.9: Reconstructed shower energy versus shower depth for photon Monte Carlo (top left), proton Monte Carlo (top right) and data (bottom). The red line indicates the applied cut on this variable calculated as shown in Equation 4.11 and the events above this red line are discarded.

is used and this cut is shown with a red line in these plots.

Shower depth is another parameter related to the particle showers, calculated using the radiation length. In order to calculate this variable, critical energy, the energy at which Bremsstrahlung and ionization rates are equal, is needed. The critical energy is calculated approximately with the formula:

$$E_c = \frac{800MeV}{Z + 1.2} \tag{4.9}$$

After the calculation of the critical energy, the shower depth is calculated according to the equation:

$$X = X_0 \frac{\ln(E/E_c)}{ln2} \tag{4.10}$$

As can be deduced from the equation, it is energy dependent and the cut applied on

this parameter is as as follows:

$$\text{Shower Depth} = -5.00 - 2.42 \cdot log_{10}(E_{rec}) \quad (cm) \tag{4.11}$$

The variable and the applied cut can be seen in Figure 4.9.

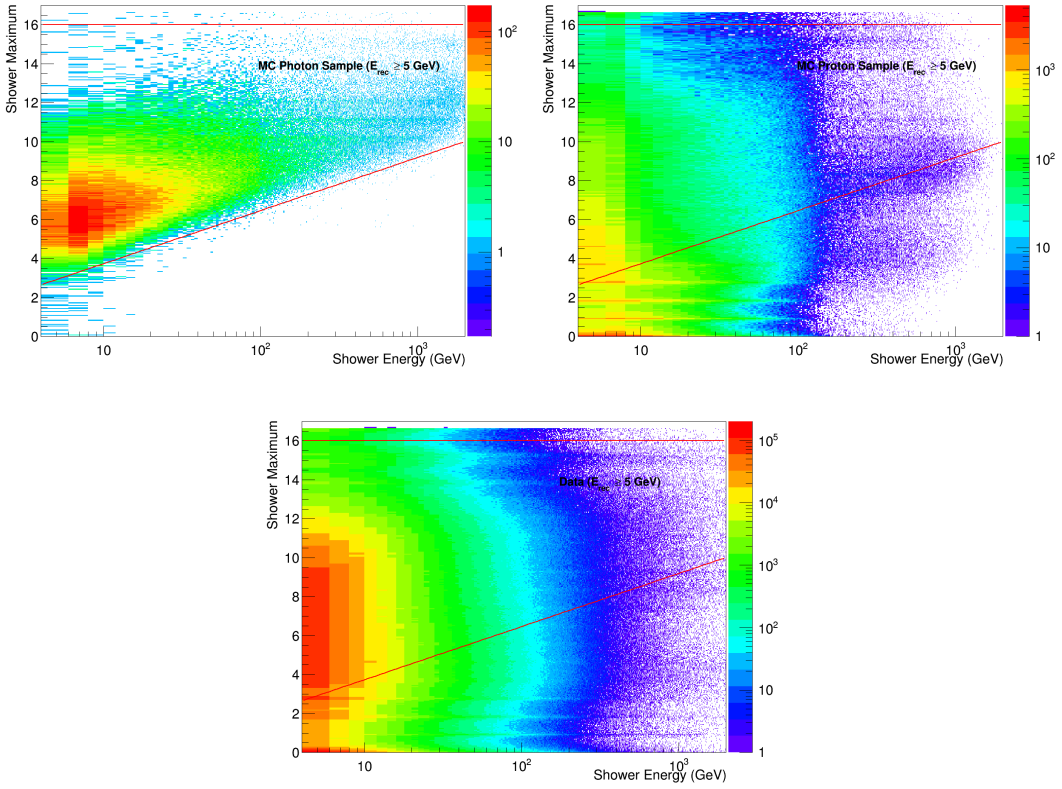

Figure 4.10: Reconstructed shower energy versus shower maximum for photon Monte Carlo (top left), proton Monte Carlo (top right) and data (bottom). The red lines indicate the applied cuts on this variable calculated as shown in Equation 4.12 and the events outside these red lines are discarded.

Particle showers start with small energy depositions, increase as the matter is traversed and finally decrease as it expires. The longitudinal location where the energy deposition reaches a peak value is defined as the shower maximum. Shower maximum is a variable which is effective for differentiating photons from protons. The photon penetration depends on energy while the shower maximum for protons does not. This can be used to eliminate the proton background especially at high energies with cuts selected as:

$$1.00 + 2.73 \cdot log_{10}(E_{rec}) < \text{Shower Maximum} < 16.00 \quad (n.u.) \tag{4.12}$$

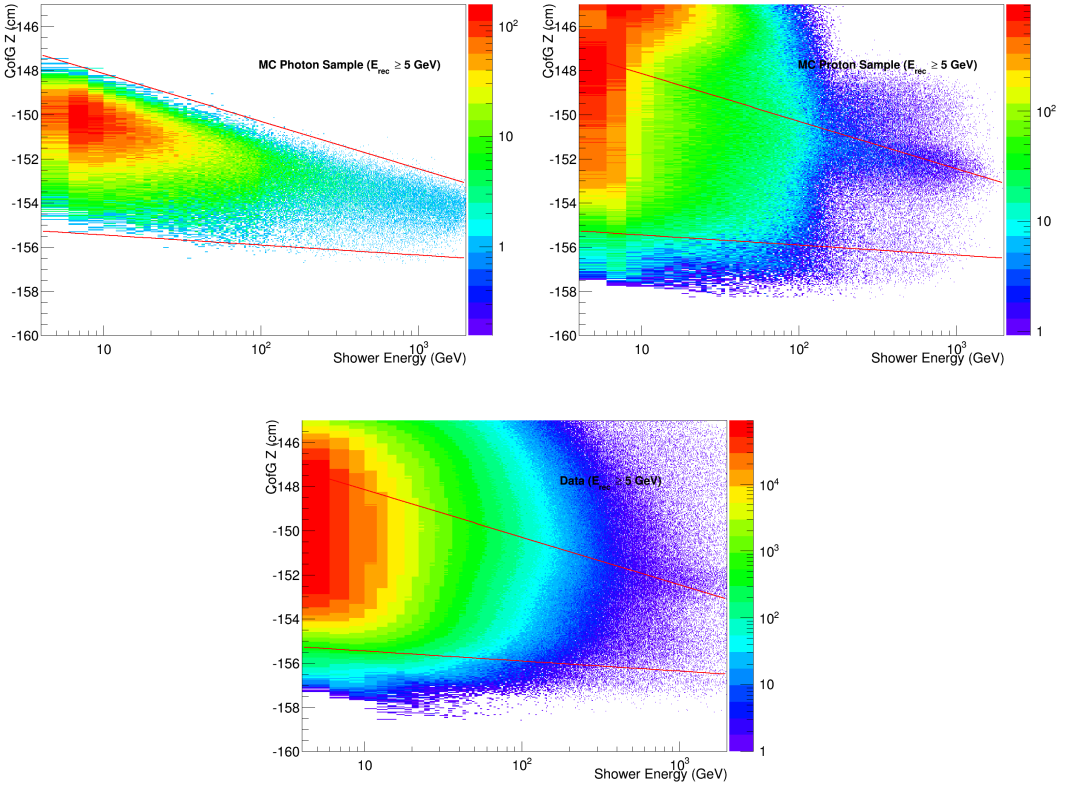

Figure 4.11: Reconstructed shower energy versus centre of gravity in $\hat{z}$ direction for photon Monte Carlo (top left), proton Monte Carlo (top right) and data (bottom). The red lines indicate the applied cuts on this variable calculated as shown in Equation 4.14 and the events outside these red lines are discarded.

The shower maximum can be seen in Figure 4.10.

From the one dimensional clusters in each layer, unique weighted relative position in $\hat{z}$ direction of the distribution of energy where it sums up to zero is calculated according to the formula

$$CofG - Z = \frac{\sum_{1DCluster} \cdot (E_{1DCluster} \cdot Layer_{1DCluster})}{\sum_{1DCluster} \cdot E_{1DCluster}} \tag{4.13}$$

and is named the centre of gravity in the $\hat{z}$ direction in units of cm. This average is different for photons and protons because even though photon showers begin early in the calorimeter, since the nuclear interaction length is not enough, protons shower late or they do not shower at all. The cuts on this variable are as follow:

$$-155.00 - 0.45 \cdot log_{10}(E_{rec}) < \text{CofG}$$

$$< -146.00 - 2.15 \cdot log_{10}(E_{rec}) \quad (cm) \tag{4.14}$$

Figure 4.11 shows histograms of this variable with respect to reconstructed energy.

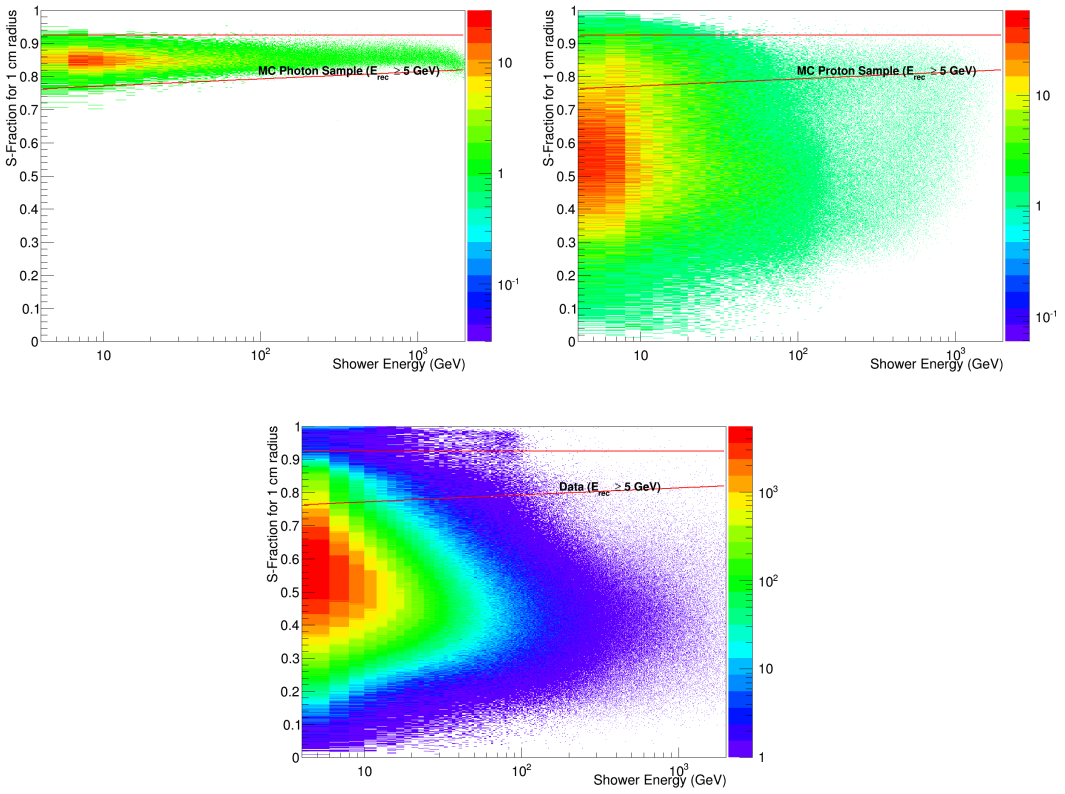

Figure 4.12: Reconstructed shower energy versus fraction of energy deposition of 1 cm radius circle for photon Monte Carlo (top left), proton Monte Carlo (top right) and data (bottom). The red lines indicate the applied cuts on this variable calculated as shown in Equation 4.15 and the events outside these red lines are discarded.

Hadronic particles such as protons radiate more particles to the calorimeter compared to the photons which interact to give electrons and positrons, as well as low energy photons. This leads to larger amounts of energy depositions in each layer for hadronic particles. Fraction of energy deposition in layers of ECAL can be used as a differentiating parameter. The fraction of energy depositions in the surrounding cells to that of the cell with the highest energy deposition in a layer is called the S-fraction. This parameter around this central cell is calculated for such as $1\ cm$, $3\ cm$ and $5\ cm$ and is used for particle discrimination. The S-fractions for each ECAL layer is summed and then divided by the reconstructed shower energy. The histograms in Figure 4.12, Figure 4.13 and Figure 4.14 show these fractions for $1\ cm$, $3\ cm$, $5\ cm$ and they demonstrate the high separation powers of this variable for photons and protons.

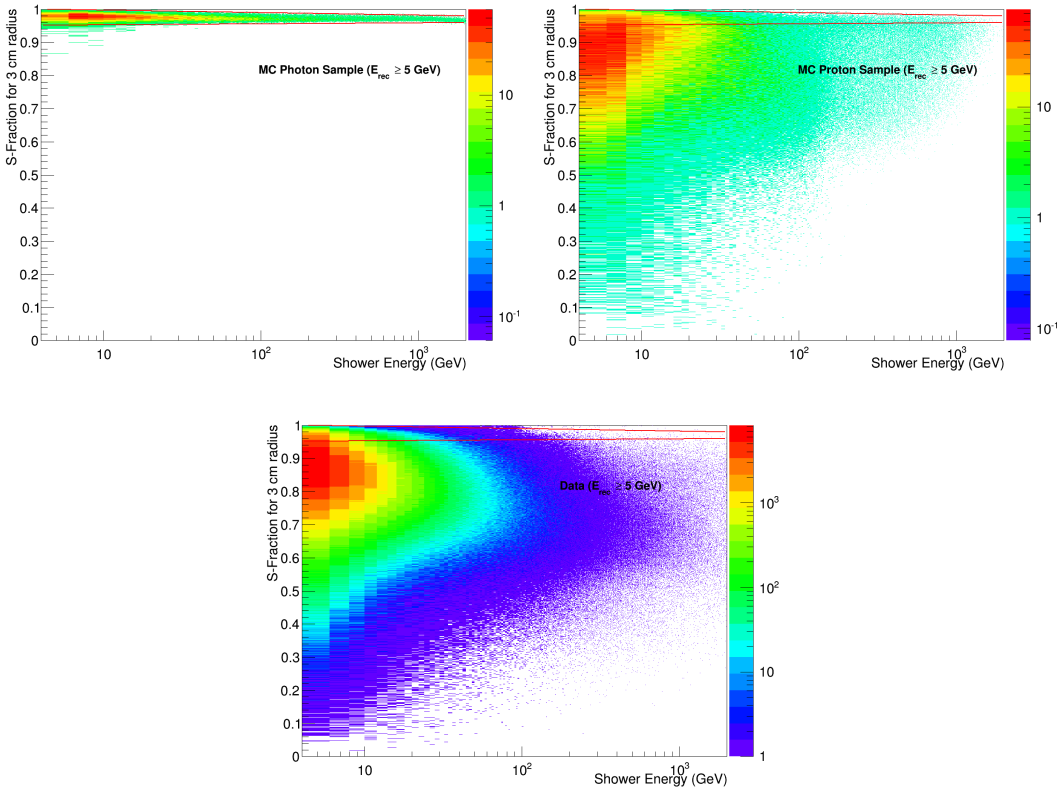

Figure 4.13: Reconstructed shower energy versus fraction of energy deposition of 3 cm radius circle for photon Monte Carlo (top left), proton Monte Carlo (top right) and data (bottom). The red lines indicate the applied cuts on this variable calculated as shown in Equation 4.16 and the events outside these red lines are discarded.

Cuts applied on 1 cm S-fraction are as follow:

$$0.750 + 0.021 \cdot log_{10}(E_{rec}) < \text{1 cm S-frac} < 0.925 \quad (n.u.) \tag{4.15}$$

Cuts applied on 3 cm S-fraction are as follow:

$$0.950 + 0.003 \cdot log_{10}(E_{rec}) < \text{3 cm S-frac}$$

$$< 1.01 - 0.01 \cdot log_{10}(E_{rec})(n.u.) \tag{4.16}$$

Cuts applied on 5 cm S-fraction are as follow:

$$0.980 + 0.001 \cdot log_{10}(E_{rec}) < \text{5 cm S-frac}$$

$$< 1.008 - 0.004 \cdot log_{10}(E_{rec}) \quad (n.u.) \tag{4.17}$$

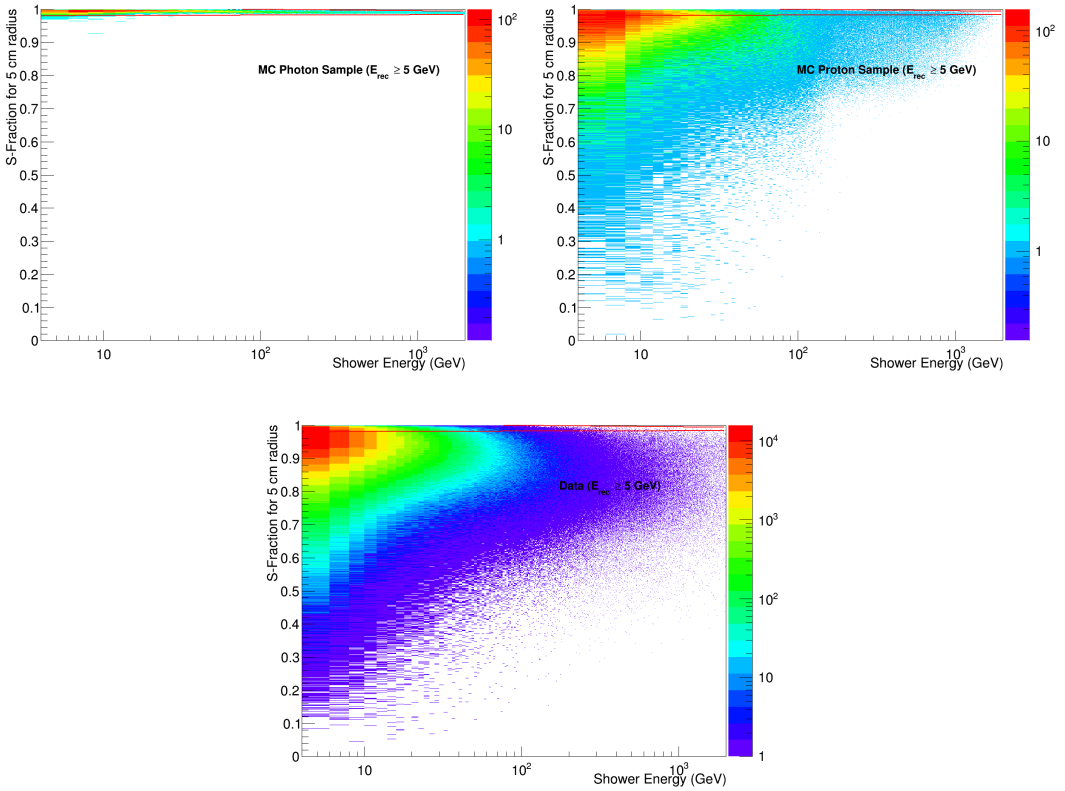

Figure 4.14: Reconstructed shower energy versus fraction of energy deposition of 5 cm radius circle for photon Monte Carlo (top left), proton Monte Carlo (top right) and data (bottom). The red lines indicate the applied cuts on this variable calculated as shown in Equation 4.17 and the events outside these red lines are discarded.

Another parameter that is used in the analysis is shower footprint. It gives the determinant of the inertia tensor for the shower and in its calculation, energy deposition in each cell, cell numbers and layer numbers are used:

$$\sigma_X = \sum (Cell - Cell_{CofG-X})^2 \cdot EDep_{Layer,Cell} \tag{4.18}$$

$$\sigma_{XZ} = \sum (Cell - Cell_{CofG-X}) \cdot (Layer - Layer_{CofG-Z}) \cdot EDep_{Layer,Cell} \tag{4.19}$$

$$\sigma_{Z^2X} = \sum (Layer - Layer_{CofG-Z})^2 \cdot EDep_{Layer,Cell} \tag{4.20}$$

$$\text{Shower Footprint X} = \frac{\sqrt{|\sigma X \cdot \sigma Z2_X - \sigma XZ^2|}}{\text{Total EDep - X Layers}} \tag{4.21}$$

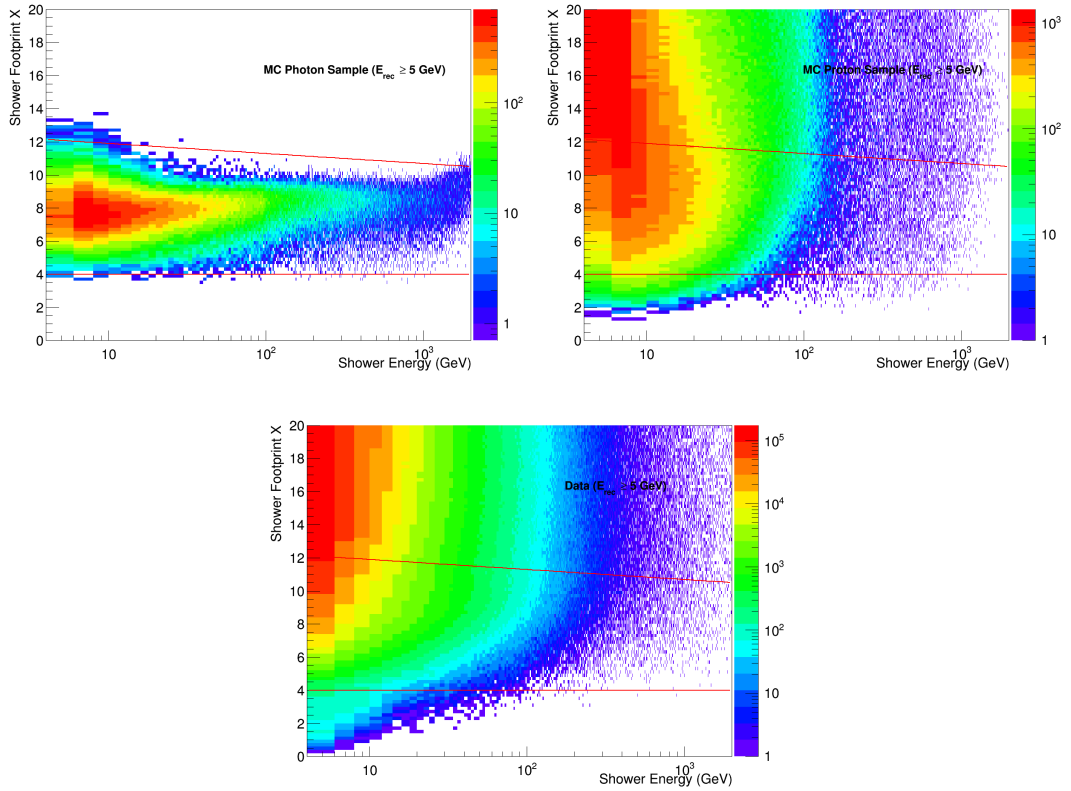

Figure 4.15: Reconstructed shower energy versus shower footprint in X layers for photon Monte Carlo (top left), proton Monte Carlo (top right) and data (bottom). The red lines indicate the applied cuts on this variable calculated as shown in Equation 4.22 and the events outside these red lines are discarded.

The shower footrint for Y layers is defined in a similar way. The equations for the cuts are as presented here:

$$4.00 < \text{Shower Footprint - X} < 12.50 - 0.61 \cdot log_{10}(E_{rec}) \quad (n.u.) \tag{4.22}$$

$$1.60 < \text{Shower Footprint - Y} < 7.80 - 0.76 \cdot log_{10}(E_{rec}) \quad (n.u.) \tag{4.23}$$

Histograms of shower footprint parameter for X and Y layers are shown in Figure 4.15 and Figure 4.16. The footprint of a photon shower is well defined and lies within certain limits. This can be used as a cut against the proton background.

Since the lateral dispersion of the energy deposition of the proton showers is expected to be bigger, it can be used to discriminate between photons and protons. The lateral dispersion can be calculated for X layers as:

$$Cell_{CofG-X} = \frac{\sum(E_{hit} \cdot Cell_{hit})}{\sum E_{hit}} \tag{4.24}$$

$$< R_X^2 >= \sum_{Layer} \frac{\sum E_{hit} \cdot (Cell_{hit} - Cell_{CofG-X})^2}{\sum E_{hit}} \tag{4.25}$$

The calculation for Y layers is similar. $< R^2 >$ terms gives the standard deviation of the lateral energy distribution. The cuts applied on lateral dispersion for X and Y layers are as follows:

$$0.3 < \text{Lateral Dispersion - X} < 2.4 \quad (n.u.) \tag{4.26}$$

$$0.3 < \text{Lateral Dispersion - Y} < 2.4 \quad (n.u.) \tag{4.27}$$

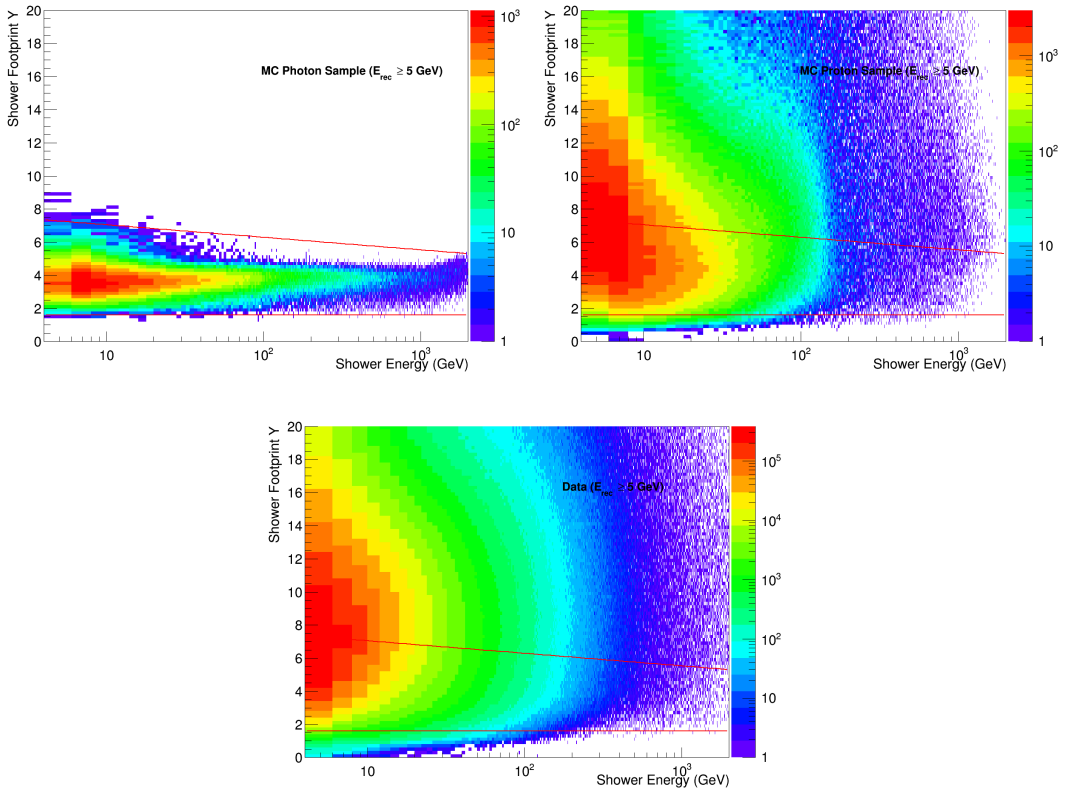

Figure 4.16: Reconstructed shower energy versus shower footprint in Y layers for photon Monte Carlo (top left), proton Monte Carlo (top right) and data (bottom). The red lines indicate the applied cuts on this variable calculated as shown in Equation 4.23 and the events outside these red lines are discarded.

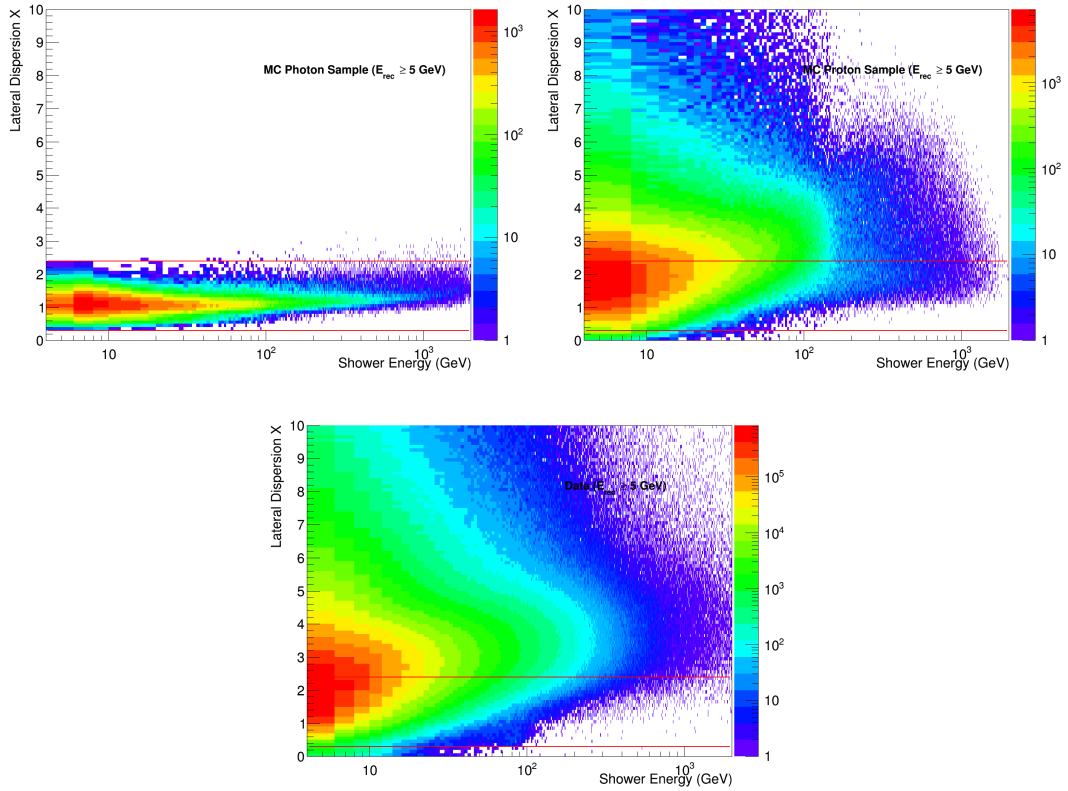

Figure 4.17: Reconstructed shower energy versus standard deviation of lateral energy distribution on X layers for photon Monte Carlo (top left), proton Monte Carlo (top right) and data (bottom). The red lines indicate the applied cuts on this variable calculated as shown in Equation 4.26 and the events outside these red lines are discarded.

Figure 4.17 and Figure 4.18 show these variables for photon and proton Monte Carlo simulations as well as data.

The last variable used in this analysis is the ECAL χ^2 method. The reconstruction for ECAL χ^2 is carried out by parametrizing the transverse shape of an electron shower for each layer with respect to energy and angle. Then, χ^2 is calculated for an arbitrary event. The applied cut on this variable is as shown here:

$$\chi^2 = 0.38462 + 0.01154 \cdot E_{rec} \quad (n.u.) \tag{4.28}$$

Figure 4.19 shows the ECAL χ^2 with respect to the reconstructed shower energy for MC photons, MC protons and data.

After all of these cuts are applied in the photon and proton Monte Carlo simulations,

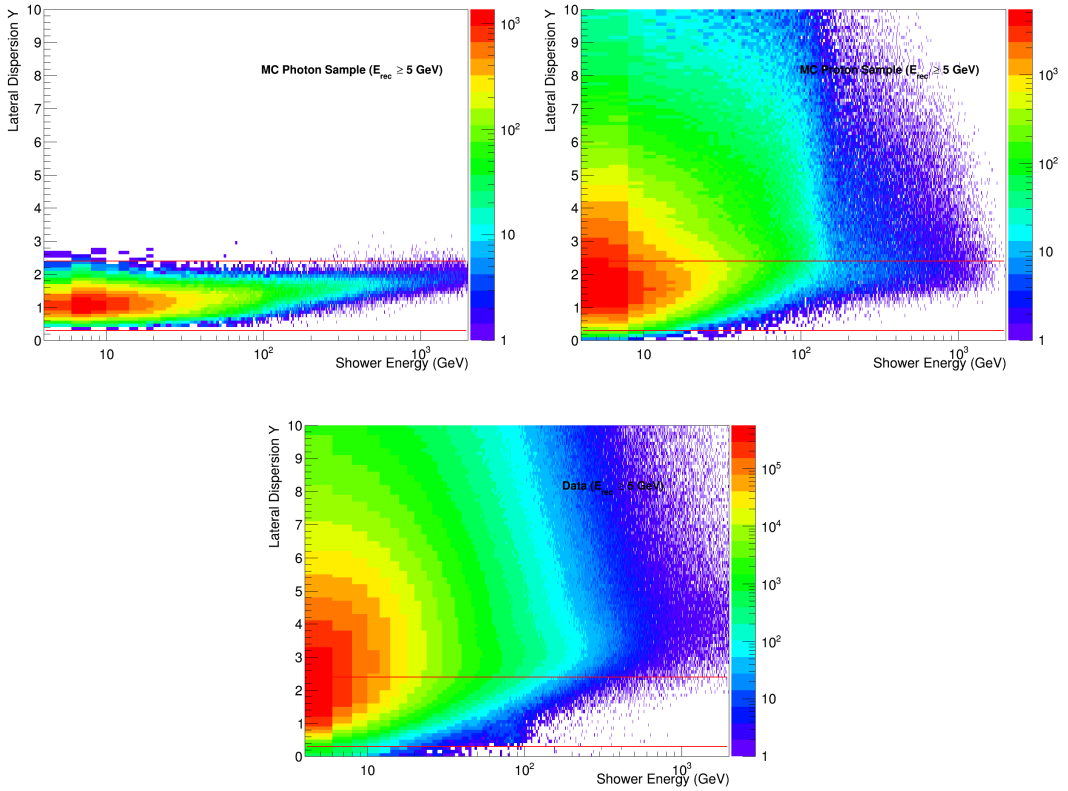

Figure 4.18: Reconstructed shower energy versus standard deviation of lateral energy distribution on Y layers for photon Monte Carlo (top left), proton Monte Carlo (top right) and data (bottom). The red lines indicate the applied cuts on this variable calculated as shown in Equation 4.27 and the events outside these red lines are discarded.

acceptances and fraction of contamination are calculated. When they are applied for data, the flux is obtained and a galactic map of photon arrival can be plotted.

4.1.2 Calculation of Acceptance

AMS-02's effective area and angle of acceptance for incident cosmic rays depend on the cuts used for the analysis. By limiting the positions and angles of the incoming particles, a purer sample of particles which pass through almost all of the subdetectors can be selected allowing to have more information on them. The geometrical area in this analysis is limited by the upper ToF layers as shown in Figure 4.20. The reason for using upper ToF layers is that the particle going through the upper ToF layers and showering in the ECAL has to traverse the active area of each sub detector which

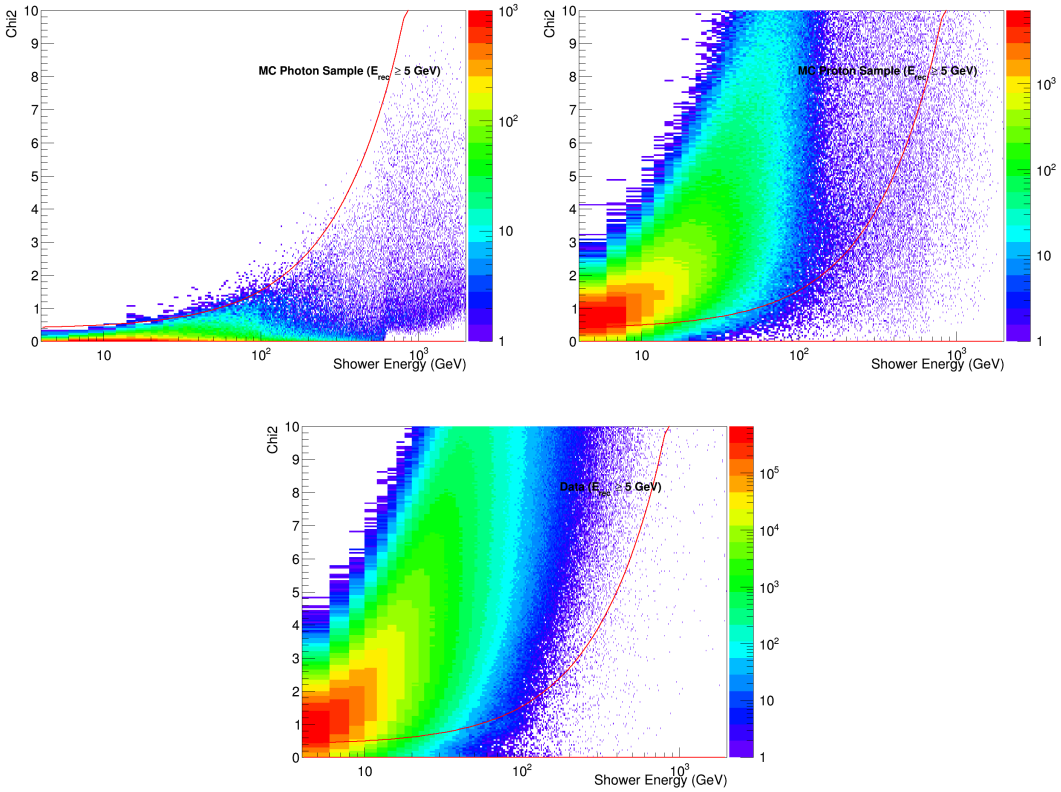

Figure 4.19: Reconstructed shower energy versus χ^2 for photon Monte Carlo (top left), proton Monte Carlo (top right) and data (bottom). The red line indicates the applied cut on this variable calculated as shown in Equation 4.28 and the events above this red line are discarded.

gives the maximum amount of information that can be retrieved for that particle.

The active area chosen is called the geometrical acceptance and measured in cm^2sr. For different analysis, acceptance is calculated with the formula

$$\text{Acceptance} = \text{Area of Generation Plane} \cdot \pi \cdot \frac{\text{Number of Selected Events}}{\text{Number of Generated Events}} \quad (4.29)$$

using Monte Carlo simulations. The Monte Carlo simulation used in this analysis generates photons above AMS-02 from a square with area of $3.9\ m \times 3.9\ m$. The π factor comes from the solid angle in which particles were generated above AMS-02. The division of number of selected events by number of generated events gives the overall efficiency. The important thing to notice is that not all generated events are triggered in AMS-02. This factor must be included in this calculation. The AMS-02 Monte Carlo files contain information on how many events were generated but

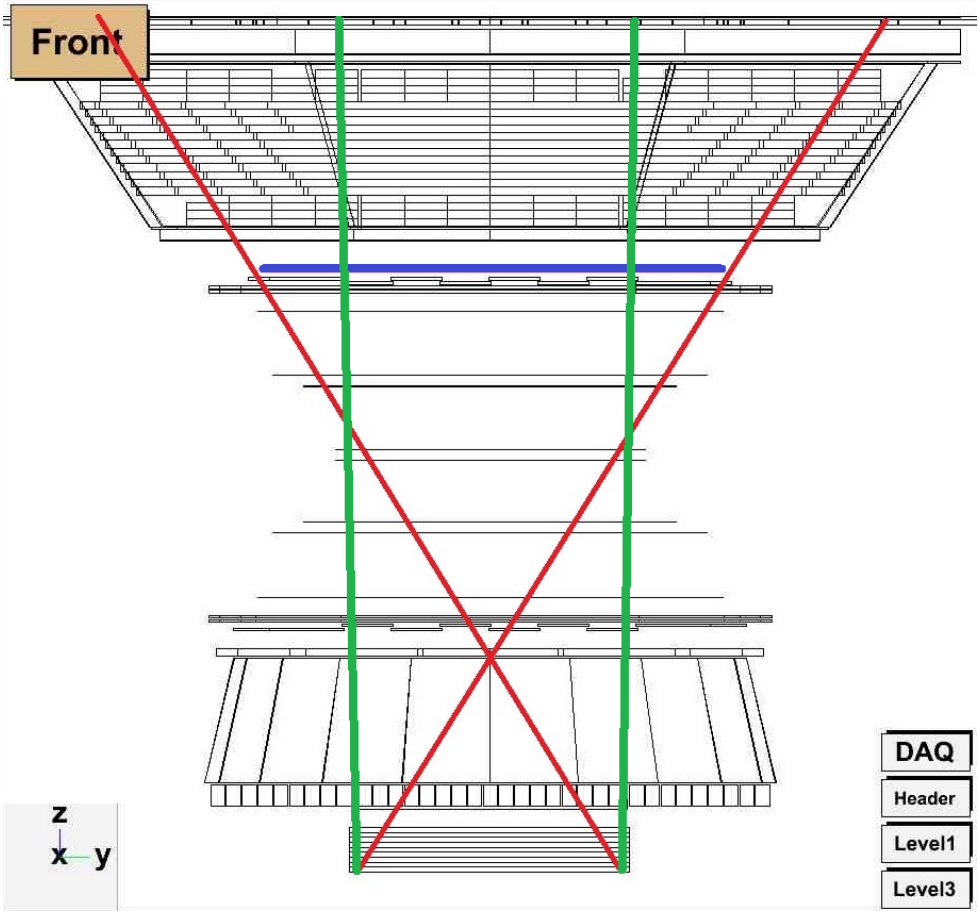

Figure 4.20: Geometry of ToF acceptance. The red lines indicate lowest and highest angle particles that are accepted from the edges of the ECAL and TOF acceptance as defined in this analysis.

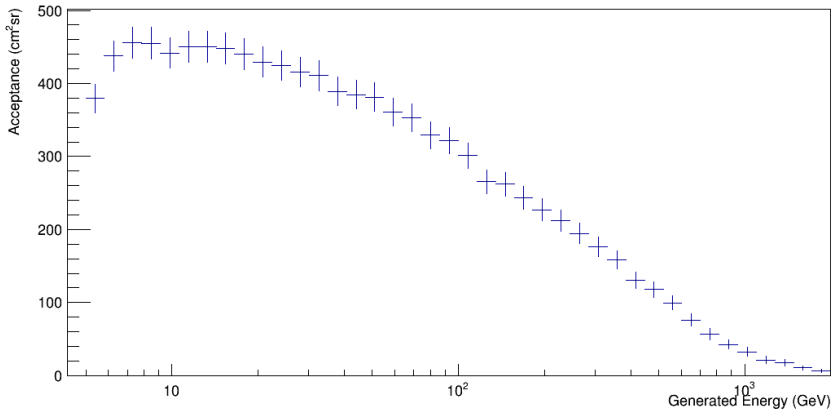

Figure 4.21: Acceptance calculated from photon Monte Carlo between $5-2000\ GeV$.

not written to disc. After the calculation is done, the resulting histogram for the acceptance is as shown in the Figure 4.21.

As can be deduced from the Figure 4.21, acceptance value below a photon energy of $100\ GeV$ is more than $400\ cm^2sr$. However, above $100\ GeV$, the acceptance decreases dramatically due to the huge amount of back scattering of particles from the ECAL at high energies and to eliminate most of the proton contamination, photons are eliminated as well.

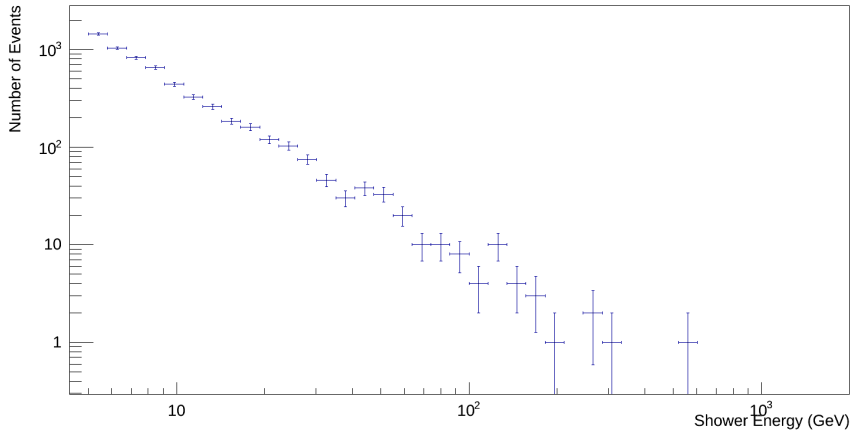

Figure 4.22: A total of 5841 candidate photon events have been identified. Shower energy is in GeV.

4.2 Results

4.2.1 Energy Spectrum and Flux of Photons in Cosmic Rays

After all of the selection cuts are applied on the AMS-02 data, the resulting energy spectrum is shown in Figure 4.22. The spectrum shows no events higher than $650\ GeV$.

After the reconstruction of the energy spectrum from data, the flux is calculated. To calculate the flux, the formula below is used:

$$\text{Flux} = \frac{\text{Energy Spectrum}}{\text{Acceptance} \cdot \text{Bin Width} \cdot \text{Measuring Time}} \tag{4.30}$$

Bin width is the difference between the edges of the consecutive bins and the unit is GeV. The measuring time is calculated from the data after all of the data quality cuts are applied and the unit for this is $seconds$. The resulting histogram for flux is shown in Figure 4.23 along with the FERMI LAT photon flux. In order to compare it with the

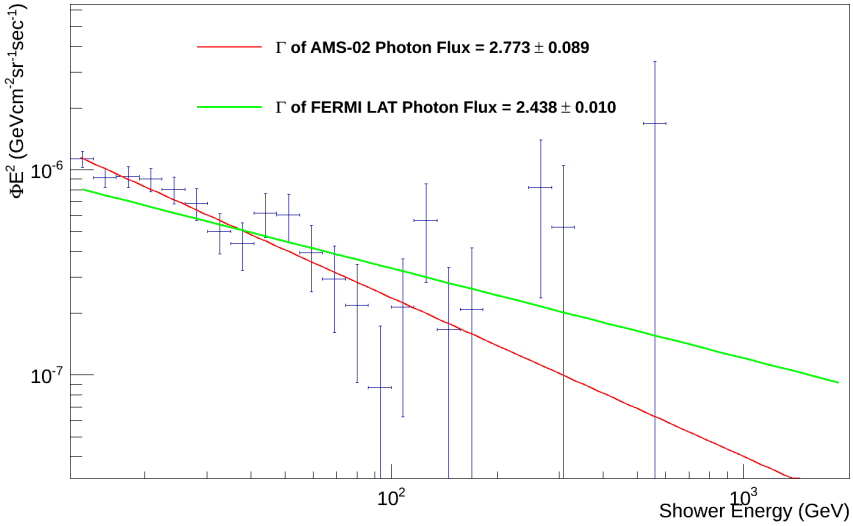

Figure 4.23: Photon flux for selected particles from data for energies above $5\ GeV$ and a comparison with the FERMI LAT flux fit. The fit for both fluxes start at $12.8\ GeV$ [8].

fit of the FERMI LAT flux, the fit for AMS-02 photon flux is carried for the candidate events above $12.8\ GeV$. Since the charged particle contamination below $10\ GeV$ is expected to be relatively high because of the particles trapped in geomagnetic field of the Earth, events below this energy is not considered in the flux calculation. The fits for two fluxes show some difference in spectral indices. The FERMI LAT used a mask to eliminate photon events from the galactic arms since the dark matter annihilations are expected to occur in the Galactic Halo and in the Galactic Center. In order to see these annihilations in the photon spectrum, the Galactic Plane except for the Galactic Center and known point sources retrieved from the source catalog of NASA were masked in the calculation of flux [41]. For the calculation of the AMS-02 flux, the same mask was used [8].

The rate at which the events arrive at AMS-02 is significant since phenomena such as solar flares can eject large amount of protons and can alter the intensity at different times. A timing study has been conducted on the selected events as shown in Figure 4.24. The histogram shows that the candidate photon events are randomly distributed in time.

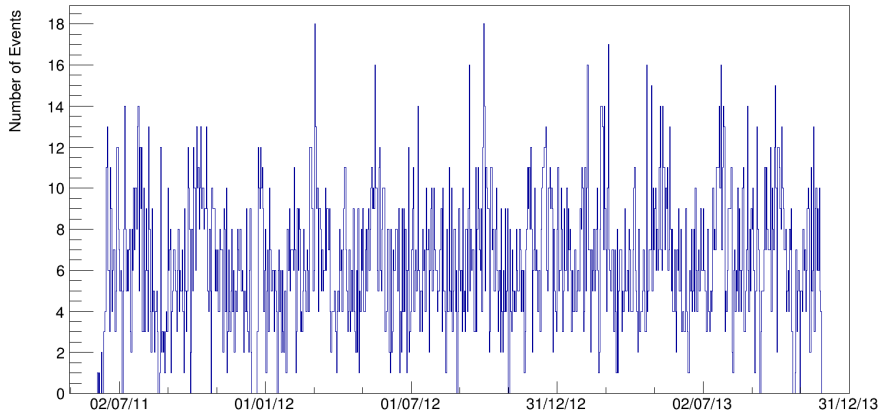

Figure 4.24: The timing information of the selected photon candidates

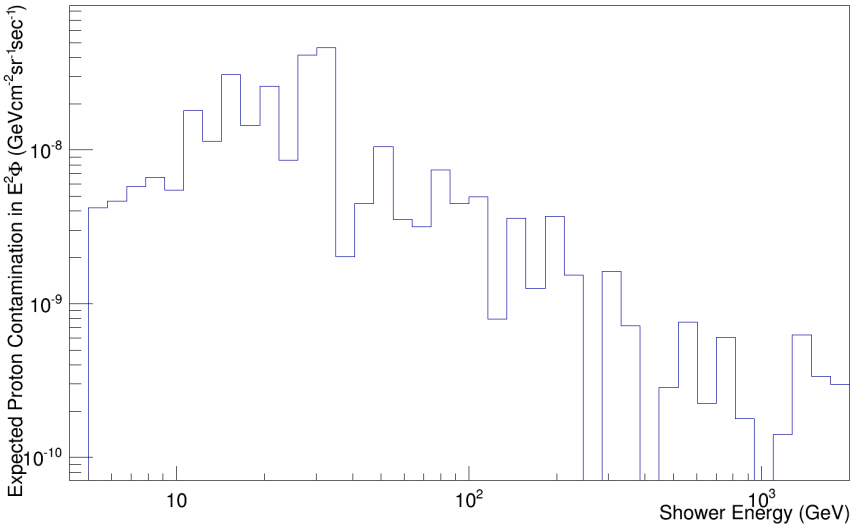

Figure 4.25: Expected proton contamination in $E^2\phi$ is obtained by multiplying the AMS-01 proton flux with proton efficiency calculated from proton MC. When compared to Figure 4.23, it can be seen that the scales of the expected proton flux is low due to high efficiency of selection [17]. The empty bins suggest the lack of events passing the selection in proton MC.

4.2.2 Calculation of Contamination

Even though multiple variables are used for eliminating background events, these particles cannot be eliminated completely and hence they contaminate the sample. Figure 4.25 shows the multiplication of the fit of the proton flux retrieved from the

AMS-01 experiment with the proton efficiency calculated from the AMS-02 proton MC [17]. This figure suggests that, since the scale is different from the photon flux of AMS-02, the proton contamination is negligible.

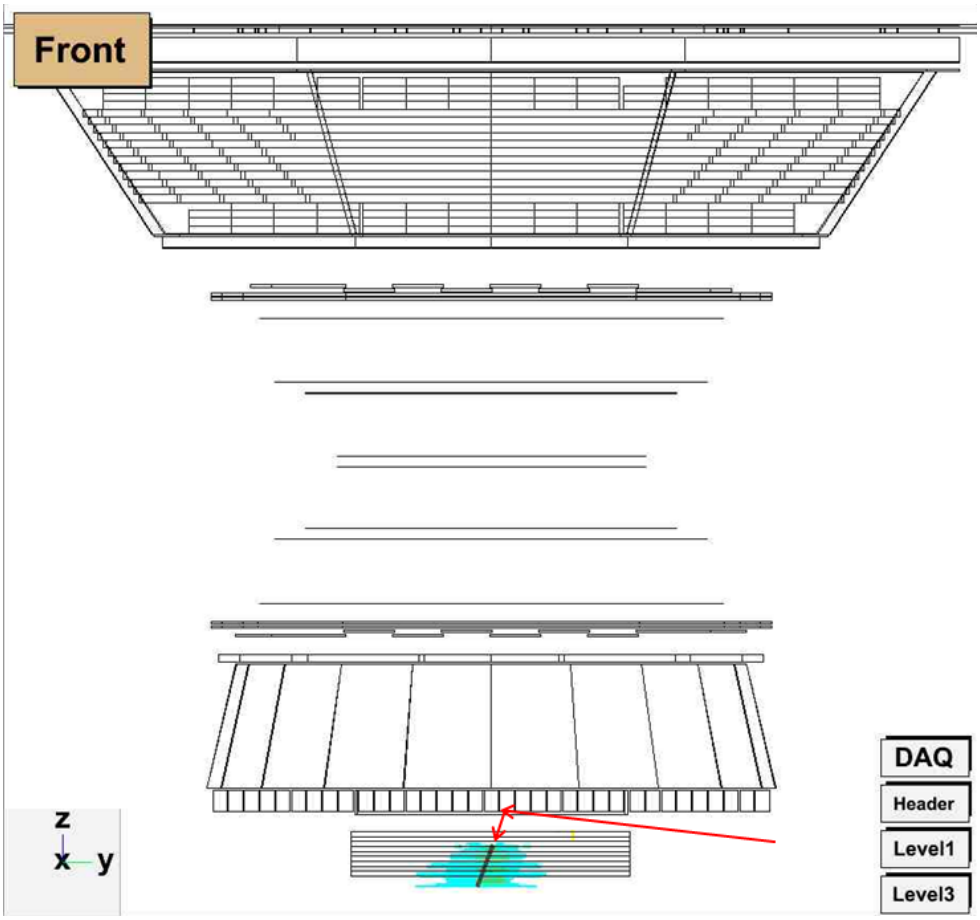

Figure 4.26: A charged particle entering through the gap between RICH and ECAL, scattering from the bottom of the RICH and showering in ECAL without interacting with other subdetectors.

However, even though the expected proton contamination is low, there are some events that may look like photons. There are various reasons for the charged particle contamination. One of the irreducible backgrounds is shown in Figure 4.26. There is a small gap between ECAL and RICH. If a particle comes from the sides and enters through this gap, then hits the bottom of the RICH, back-scatters to ECAL, this event can be observed as a calorimetric photon since it will not have any interaction with the upper subdetectors unless it back-scatters from ECAL after showering. Since there is no ACC in this part of the detector, there is no way to get rid of this type of events. Another type of contamination comes from the charged particles which are not re-

constructed as tracks in TRD, tracker and as rings in RICH due to the reconstruction efficiency of these subdetectors being less than $100\ \%$. If they are not reconstructed as tracks at the same time, and the hits or ADC counts are lower than the cut used in the analysis, then there is no way of understanding if this is a photon or a charged particle.

4.2.3 Galactic Map

The most important part of the photon analysis is to have information on the source of the incoming photons. Since photons do not bend in magnetic fields, they can be traced back to their source which in turn can hint where the dark matter annihilations in our galaxy may take place.

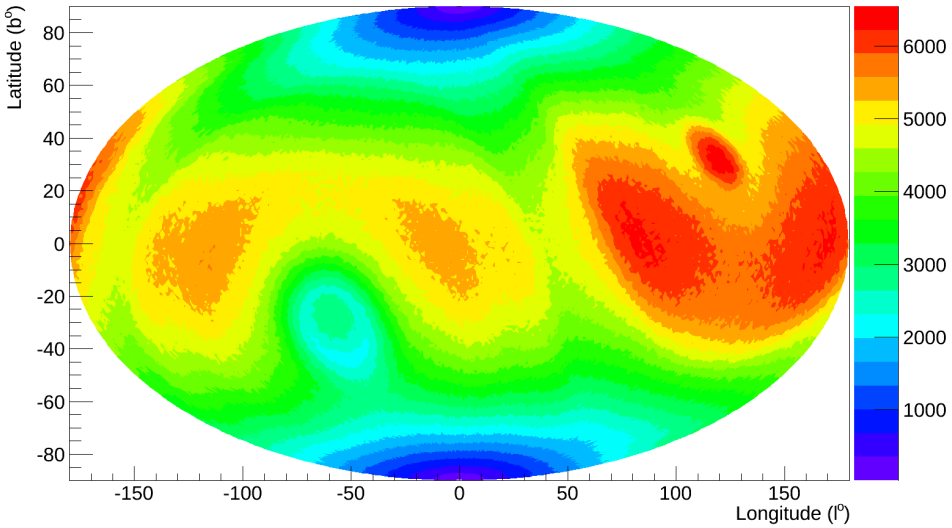

Figure 4.27: Exposure map for all particles.

Before reconstructing the galactic map, an exposure map should be drawn in order to learn about the rate at which AMS-02 is exposed to different parts of our galaxy. This map includes all of the particles in the energy range of the analysis after the data quality cuts are applied. In the Exposure Map, the $X - axis$ is the Galactic Longitude and the $Y - axis$ is the Galactic Latitude where the weights in colors give the seconds. In Figure 4.27, it can be seen that two holes which are on right above and left below do not get events as much as the other areas of the map. These two holes correspond to the North and South Poles of the Earth. Since ISS does not go

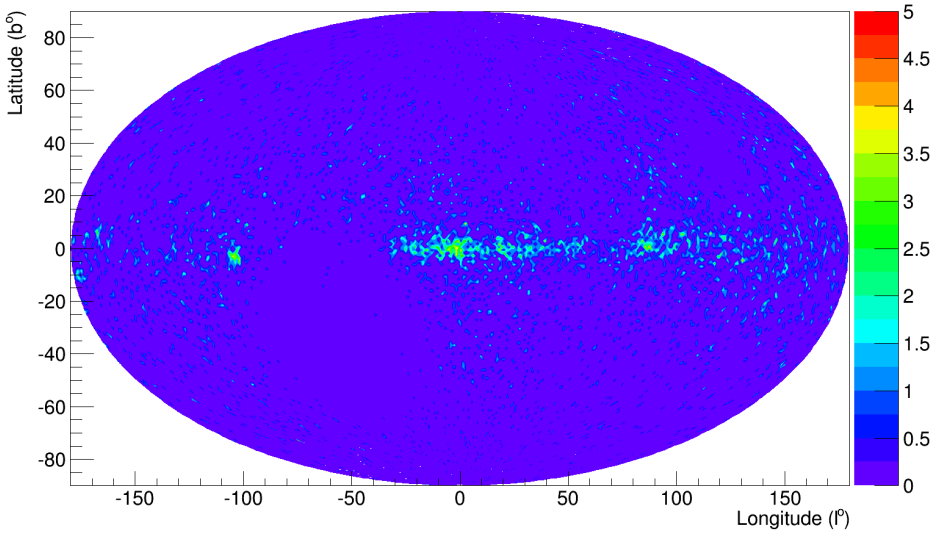

Figure 4.28: Galactic map showing 5841 photon candidates above $5\ GeV$.

through these parts of the Earth, the amount exposure is low in these areas compared to the other parts. The parts which cover these holes, where the amount of exposure is much longer, correspond to the parts of the Earth which are between the poles and the Equator, at which ISS travels through the most.

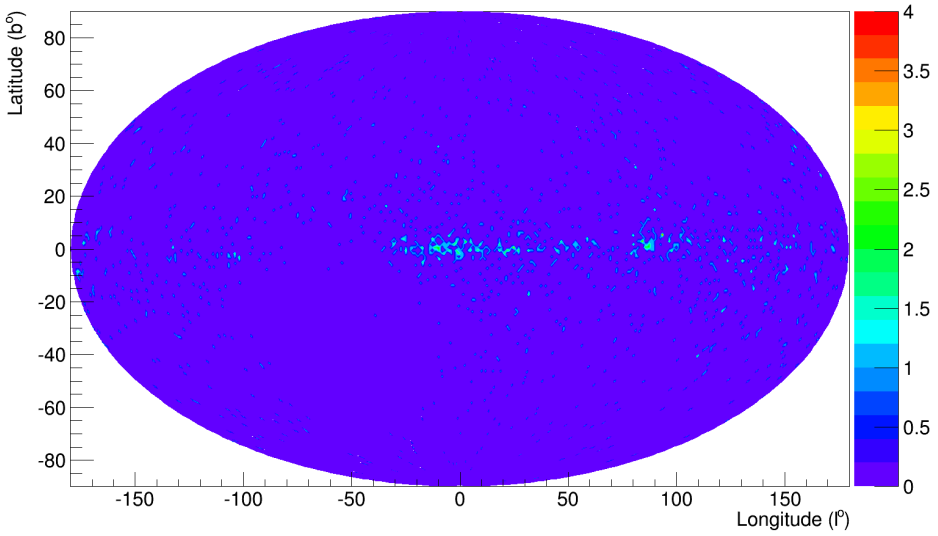

Figure 4.29: Galactic map showing 1598 photon candidates above $10\ GeV$.

After the reconstruction of the exposure map, the results of the analysis is reconstructed in a galactic map. The difference between the exposure map and the galactic map is that galactic map includes the events which are selected after all of the cuts are

applied and the weights in this map are number of events instead of sum of seconds the detector is exposed to.

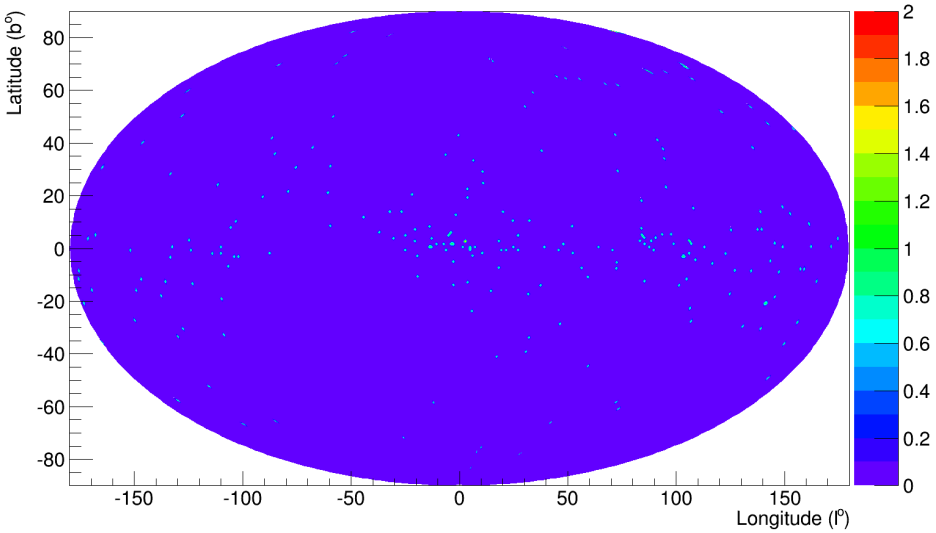

Figure 4.30: Galactic map showing 225 photon candidates above 30 GeV.

As it is shown in Figure 4.28, there are 5841 events in the energy range $5-2000\ GeV$. The concentration of the events is around the Galactic Center and along the Galactic Plane. Figure 4.29 shows the galactic map for events above $10\ GeV$ whereas Figure 4.30 shows the ones above $30\ GeV$ and Figure 4.31 above $100\ GeV$. The difference between Figure 4.28 and Figure 4.29 shows that most of the events on the Galactic Halo are between $5-10\ GeV$. If there are dark matter annihilations in the Milky Way, these are expected to be on the Galactic Halo. However, since the contamination of other particles are known to exist mostly in this energy range, this cannot give a clear picture of possible dark matter annihilations in the Galactic Halo.

There are various galactic sources included in these galactic maps. One of these sources is shown in Figure 4.32. For example, one candidate photon event was measured from $PKS1424-240$ [41].

4.2.4 Discussion of the Results

The final spectrum calculated after all of the cuts are applied includes 5841 candidate photon events above $5\ GeV$. Most of the candidate events are concentrated on the

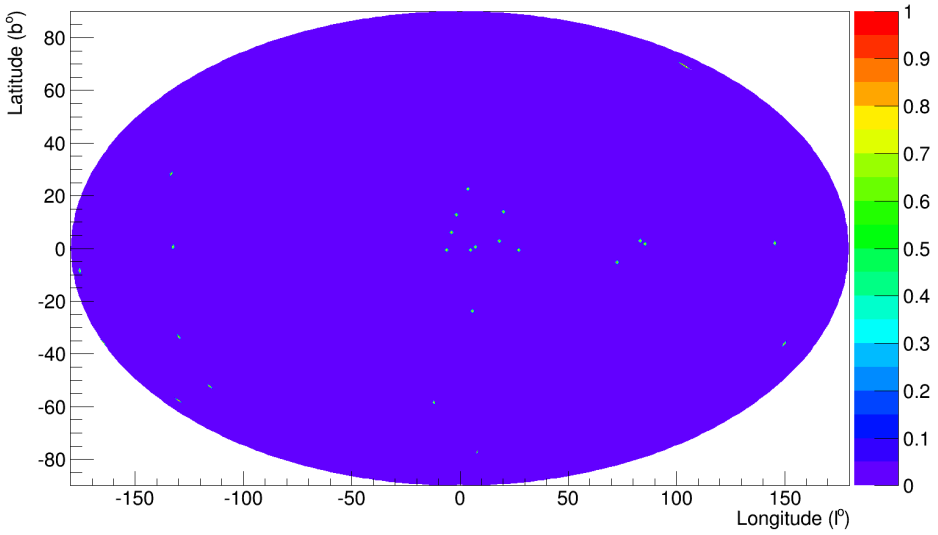

Figure 4.31: Galactic map showing 26 photon candidates above 100 GeV.

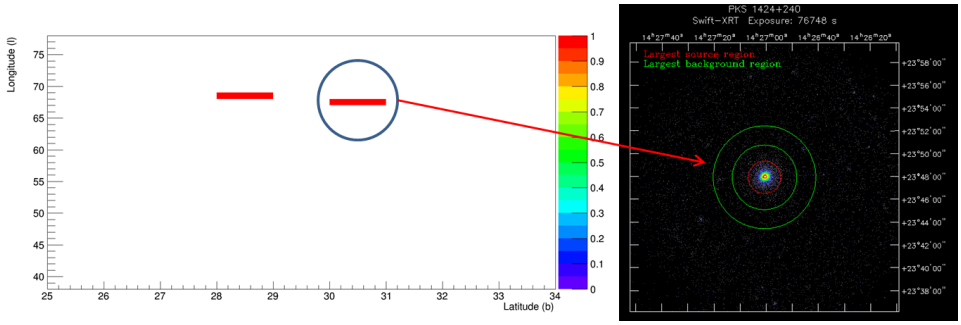

Figure 4.32: Match of an event from the AMS-02 photon events with a known source with name $PKS1424-240$ [52].

Galactic Center and along the Galactic Plane which confirms that a large amount of these particles are most likely photons. Gamma rays from known galactic sources were seen in the analysis. Energy spectrum and contamination plots suggest that, there are still other particles contaminating the results. Most of this contamination occurs in the energy region $5-10$ GeV because of the charged particles trapped in Earth's geomagnetic field. These particles could be protons tracks of which cannot be reconstructed or entering through the sides. When the reconstruction does not happen, a lack of information occurs which can cause other particles to look like photons. The error bars in the spectrum and in the flux are purely statistical. For the flux measurement, main systematic would be the absolute energy scale which has an uncertainty of 2 % at $50-80$ GeV [55].

CHAPTER 5

CONCLUSION

In this thesis, observational evidence of the existence of dark matter was presented briefly. Different search methods for detecting the particle nature of dark matter with an emphasis on detecting dark matter annihilations in gamma rays were presented. The significance and the drawbacks of gamma ray research as well as the expectations from such a research were explained. The data from the AMS-02 between May 19th, 2011 and February 28th, 2014 was used for the analysis of gamma ray spectrum in low Earth orbit.

Calorimetric mode photon analysis in this thesis mainly uses the ECAL to select photons while using other subdetectors to veto charged particles. The energy and angle information for photon candidates were retrieved from the ECAL. MC comparison of several parameters were conducted separately for photons and protons, which are the main background in this analysis. After determining the cuts, they were applied to AMS-02 data and 5841 photon candidate events were found in the energy region between $5 - 2000\ GeV$. The photon flux was calculated and compared with the FERMI LAT flux [8]. The comparison shows a small difference in the spectral index of the fits. The flux calculated in this analysis decreases more steeply than FERMI LAT flux.

REFERENCES

[1] Georges Aad et al. Search for supersymmetry using final states with one lepton, jets, and missing transverse momentum with the ATLAS detector in $\sqrt{s} = 7$ TeV pp. *Phys.Rev.Lett.*, 106, 2011.

[2] Georges Aad et al. Search for direct production of charginos, neutralinos and sleptons in final states with two leptons and missing transverse momentum in pp collisions at $\sqrt{s} = 8$ TeV with the ATLAS detector. *JHEP*, 1405:071, 2014.

[3] M.G. Aartsen et al. IceCube Search for Dark Matter Annihilation in nearby Galaxies and Galaxy Clusters. *Phys.Rev.*, D88(12):122001, 2013.

[4] Abdo et al. Fermi LAT Search for Photon Lines from 30 to 200 GeV. *Physical Review Letters*, 104, 2010.

[5] Accardo et al. High Statistics Measurement of the Positron Fraction in Primary Cosmic Rays of 0.5-500 GeV with the Alpha Magnetic Spectrometer on the International Space Station. *Phys.Rev.Lett.*, 113:121101, September 2014.

[6] Ackerman et al. Measurement of Separate Cosmic-Ray Electron and Positron Spectra with the Fermi Large Area Telescope. *Phys.Rev.Lett.*, 108:081102, September 2012.

[7] Ackermann et al. Fermi LAT observations of cosmic-ray electrons from 7 GeV to 1 TeV. *Phys. Rev. D*, 82:092004, Nov 2010.

[8] Ackermann et al. Fermi LAT search for dark matter in gamma-ray lines and the inclusive photon spectrum. *Phys.Rev.D*, 86(2):022002, July 2012.

[9] P.A.R. Ade et al. Planck 2013 results. i. overview of products and scientific results. 2013.

[10] O. Adriani et al. Cosmic-ray positron energy spectrum measured by PAMELA. *Phys. Rev. Lett.*, 111:081102, Aug 2013.

[11] Aguilar et al. Leptons in near earth orbit. *Phys. Lett. B*, 484:10, 2000.

[12] Aguilar et al. Electron and Positron Fluxes in Primary Cosmic Rays Measured with the Alpha Magnetic Spectrometer on the International Space Station. *Phys.Rev.Lett.*, 113:121102, September 2014.

[13] Aguilar et al. Precision measurement of the $(e^+ + e^-)$ flux in primary cosmic rays from 0.5 GeV to 1 TeV with the Alpha Magnetic Spectrometer on the International Space Station. *Phys. Rev. Lett.*, 113:221102, Nov 2014.

[14] M. Aguilar et al. First Result from the Alpha Magnetic Spectrometer on the International Space Station: Precision Measurement of the Positron Fraction in Primary Cosmic Rays of 0.5-350 GeV. *Phys.Rev.Lett.*, 110:141102, 2013.

[15] Aharonian, F. et al. Energy spectrum of cosmic-ray electrons at TeV energies. *Phys. Rev. Lett.*, 101:261104, Dec 2008.

[16] Aharonian, F. et al. Probing the ATIC peak in the cosmic-ray electron spectrum with H.E.S.S. *A&A*, 508(2):561–564, 2009.

[17] J. Alcaraz et al. Cosmic protons. *Physics Letters B*, 490:27–35, September 2000.

[18] P. Battinelli and S. Demers. The C star population of DDO 190. *A&A*, 447:473–480, February 2006.

[19] D. Berge. Development of an algorithm for the shower reconstruction with the h.e.s.s telescope system. Nov 2002.

[20] B. Bertucci on behalf of the AMS Collaboration. Precision measurement of the e^+ + e^- spectrum with AMS. *33rd International Cosmic Ray Conference, The Astroparticle Physics Conference*, 2013.

[21] Boezio et al. The Cosmic-Ray Electron and Positron Spectra Measured at 1 AU during Solar Minimum Activity. *Astrophys. J.*, 532:653, 2000.

[22] T. Bringmann and F. Calore. On the Relevance of Sharp Gamma-Ray Features for Indirect Dark Matter Searches. *Phys. Rev. D*, Dec 2011.

[23] T. Bringmann and C. Weniger. Gamma ray signals from dark matter: Concepts, status and prospects. Dec 2012.

[24] Bucci et al. The AMS-02 Transition Radiation Detector to Search for Dark Matter in Space. 2010.

[25] M. Buénerd. The RICH counter of the AMS experiment. *Nucl. Instrum. Meth.*, A502:158–162, 2003.

[26] J. Chang et al. An excess of cosmic ray electrons at energies of 300-800[thinsp]gev. *Nature*, 456(7220):362–365, Nov 2008.

[27] V. Choutko on behalf of the AMS Collaboration. Precision measurement of the cosmic ray helium flux with AMS experiment. *33rd International Cosmic Ray Conference, The Astroparticle Physics Conference*, 2013.

[28] D. Clowe et al. A direct empirical proof of the existence of dark matter. *Astrophys.J.*, 648:L109–L113, 2006.

[29] A. Contin and D. Grandi. South atlantic anomaly definition, June 2012.

[30] T. Daylan. Photon proton separation using Alpha Magnetic Spectrometer 02. Bachelor's Thesis, METU.

[31] T. Daylan et al. The characterization of the gamma-ray signal from the central milky way: A compelling case for annihilating dark matter. Feb 2014.

[32] B. Demirköz. A transition radiation detector and gas supply system for AMS. Master's thesis, Massachusetts Institute of Technology, 2004.

[33] DuVernois et al. Cosmic-Ray Electrons and Positrons from 1 to 100 GeV: Measurements with HEAT and Their Interpretation. *Astrophys. J.*, 559:296, 2001.

[34] M. A. DuVernois et al. Cosmic-ray electrons and positrons from 1 to 100 GeVi: Measurements with HEAT and their interpretation. *The Astrophysical Journal*, 559(1):296, 2001.

[35] C. W. Fabjan and F. Gianotti. Calorimetry for particle physics. Oct 2003.

[36] Grimani et al. Measurements of the absolute energy spectra of cosmic-ray positrons and electrons above 7 GeV. *Astron. Astrophys.*, 392:287, September 2002.

[37] Gerard Jungman, Marc Kamionkowski, and Kim Griest. Supersymmetric dark matter. *Physics Reports*, 267(5–6):195 – 373, 1996.

[38] V. Khachatryan et al. Searches for electroweak production of charginos, neutralinos, and sleptons decaying to leptons and W, Z, and Higgs bosons in pp collisions at 8 TeV. May 2014.

[39] A. Kounine on behalf of the AMS Collaboration. Precision measurement of the positron fraction in primary cosmic rays of 0.5-350 GeV. *33rd International Cosmic Ray Conference, The Astroparticle Physics Conference*, 2013.

[40] William R. Leo. Techniques for nuclear and particle physics experiments. 1987.

[41] Fermi Gamma-Ray Telescope NASA. LAT 4-year Point Source Catalog (3FGL). http://fermi.gsfc.nasa.gov/ssc/data/access/lat/, last accessed on 24.02.2015.

[42] A. Oliva on behalf of the AMS Collaboration. Precision measurement of the cosmic ray boron-to-carbon ratio with AMS. *33rd International Cosmic Ray Conference, The Astroparticle Physics Conference*, 2013.

[43] R.D. Peccei and Helen R. Quinn. CP Conservation in the Presence of Instantons. *Phys.Rev.Lett.*, 38:1440–1443, 1977.

[44] E. Postacı. Conversion mode photon analysis using the alpha magnetic spectrometer (ams-02). Jul 2014.

[45] V.C. Rubin, N. Thonnard, and Jr. Ford, W.K. Rotational properties of 21 SC galaxies with a large range of luminosities and radii, from NGC 4605 /R = 4kpc/ to UGC 2885 /R = 122 kpc/. *Astrophys.J.*, 238:471, 1980.

[46] Vera C. Rubin and W. Kent Ford, Jr. Rotation of the Andromeda Nebula from a Spectroscopic Survey of Emission Regions. *Astrophys.J.*, 159:379–403, 1970.

[47] Tarek Saab. An Introduction to Dark Matter Direct Detection Searches & Techniques. 2012.

[48] The AMS Collaboration. http://ams.cern.ch, last accessed on 25.02.2015.

[49] The AMS Collaboration. AMS on ISS Construction of a particle physics detector on the International Space Station. *AMS Note*, 2004.

[50] The ICECUBE Collaboration. https://icecube.wisc.edu/, last accessed on 20.01.2015.

[51] The Particle Data Group. Passage of particles through matter. http://pdg.lbl.gov/, last accessed on 08.02.2015.

[52] Penn State University - The Swift Gamma Ray Explorer. Swift-XRT Monitoring of Fermi-LAT Sources of Interest. http://www.swift.psu.edu/monitoring/source.php?source=PKS1424+240, last accessed on 09.03.2015.

[53] Samuel Ting. New Results from the Alpha Magnetic Spectrometer on the International Space Station. Sep 2014.

[54] S. Torii et al. The energy spectrum of cosmic-ray electrons from 10 to 100 GeV observed with a highly granulated imaging calorimeter. *The Astrophysical Journal*, 559(2):973, 2001.

[55] Vecchi et al. The electromagnetic calorimeter of the AMS-02 experiment.

[56] C. Weniger. A Tentative Gamma-Ray Line from Dark Matter Annihilation at the Fermi Large Area Telescope. *Phys. Rev. D*, Aug 2012.

[57] K. Yoshida et al. Cosmic-ray electron spectrum above 100 GeV from PPB-BETS experiment in Antarctica. *Advances in Space Research*, 42(10):1670 – 1675, 2008.

[58] F. Zwicky. On the Masses of Nebulae and of Clusters of Nebulae. *Astrophys.J.*, 86:217–246, 1937.